Mon. Not. R. Astron. Soc. **000**, 000–000 (0000) Printed 27 June 2013 (MN LATEX style file v2.2)

The physical nature of the 8 o'clock arc based on near-IR IFU spectroscopy with SINFONI⋆

M. Shirazi[1]†, S. Vegetti[2,3], N. Nesvadba[4], S. Allam[5,6], J. Brinchmann[1], D. Tucker[5]
[1] *Leiden Observatory, Leiden University, P.O. Box 9513, 2300 RA Leiden, The Netherlands*
[2] *Kavli Institute for Astrophysics and Space Research,Massachusetts Institute of Technology, Cambridge, MA 02139, USA*
[3] *Max-Planck Institute for Astrophysics, Karl-Schwarzschild-Strasse 1, 85740 Garching, Germany*
[4] *Institut d'Astrophysique Spatiale, UMR 8617, CNRS, Université Paris-Sud, Bâtiment 121, 91405, Orsay Cedex, France*
[5] *Fermi National Accelerator Laboratory, P.O. Box 500, Batavia, IL 60510, USA*
[6] *Space Telescope Science Institute, 3700 San Martin Drive, Baltimore, MD 21218*

27 June 2013

ABSTRACT

We present an analysis of near-infrared integral field unit spectroscopy for the gravitationally lensed Lyman break galaxy, the 8 o'clock arc, taken with SINFONI on the Very Large Telescope. We explore the shape of the spatially-resolved Hβ profile and demonstrate that we can decompose it into three main components that partially overlap (spatially) but are distinguishable when we include the dynamical information. To study the de-lensed morphology of the galaxy we make use of existing B & H imaging from the *Hubble Space Telescope* and construct a rigorous lens model using a Bayesian grid based lens modeling technique. We apply this lens model to the SINFONI data cube to construct the de-lensed Hβ line map and the velocity and velocity dispersion maps of the galaxy. We explore the dynamical state of the galaxy and find that the 8 o'clock arc has a complex velocity field that is not simply explained by a single rotating disk. The Hβ profile of the galaxy shows a blue-shifted wing suggesting gas outflows of $\sim$ 200 km s^{-1}. We confirm previous findings that the 8 o'clock arc lies on the stellar mass–oxygen abundance–star formation rate plane found locally, but it has nevertheless significantly different interstellar medium properties. We show that the gas surface density of the 8 o'clock arc is a factor of 2–4 higher than similar low-redshift galaxies selected from the Sloan Digital Sky Survey. We also find that the electron density in the ionized gas is approximately five times higher than in the comparison sample, which implies a higher H II-region pressure as well as likely a higher density interstellar medium than in similar nearby galaxies.

Key words: galaxies: evolution — galaxies: formation — galaxies: high-redshift — galaxies: kinematics and dynamics — galaxies: ISM — gravitational lensing: strong

1 INTRODUCTION

The last decade has seen a dramatic increase in our knowledge of the galaxy population at redshift $z > 2$. In particular, the large samples of high redshift (high-z) galaxies identified by the Lyman-break dropout technique (Steidel et al. 2003, and references therein) have allowed detailed statistical analysis of the physical properties of these galaxies (Shapley 2011). While early studies made use of long-slit near-IR spectroscopy (Erb et al. 2006a,b,c) to study the physical properties of these galaxies, more recent studies have focused on near-IR integral field units (IFUs) (Förster Schreiber et al. 2006, 2009; Genzel et al. 2008, 2010).

The steadily growing effort to obtain resolved near-IR spectra of high-z galaxies in a systematic manner as in the MASSIV, SINS, SINS/zC-SINF and LSD/AMAZE surveys is leading to samples of spatially-resolved emission line maps of distant ($z \sim 1-3.8$) star-forming galaxies. Studying these maps has provided us with spatially-resolved physical properties, metallicity gradients and kinematics of high-z star-forming galaxies (e.g., Contini et al. 2012; Epinat et al. 2012; Förster Schreiber et al. 2009; Cresci et al. 2009;

⋆ Based on observations obtained at the Very Large Telescope (VLT) of the European Southern Observatory, Paranal, Chile (ESO Program ID: 83A:0879A, PI: J. Brinchmann). Also based on observations with the NASA/ESA *Hubble Space Telescope (HST)*, obtained at the Space Telescope Science Institute under the program ID No. 11167 (PI: S. Allam).

† shirazi@strw.leidenuniv.nl

Genzel et al. 2011; Förster Schreiber et al. 2011a,b; Newman et al. 2012b; Maiolino et al. 2008; Mannucci et al. 2009; Gnerucci et al. 2011).

A particularly important question for these studies is whether the observed dynamics are due to, or significantly influenced by major mergers. While this is generally difficult to establish, Genzel et al. (2006) have shown that with sufficiently high resolution integral field unit (IFU) spectroscopy, it is possible to distinguish between rotation and merging. However, variations in spatial resolution still cause inconclusive interpretations. As an example, using SINFONI observations of 14 LBGs Förster Schreiber et al. (2006) argued for rotationally supported dynamics in many LBGs (7 out of 9 resolved velocity fields). In contrast, by studying spatially resolved spectra of 3 galaxies at redshift $z \sim 2-3$, using the OSIRIS in combination with adaptive optics (AO), Law et al. (2007) showed that the ionized gas kinematics of those galaxies were inconsistent with simple rotational support.

Analysis of the SINS Hα sample studied by Förster Schreiber et al. (2009) showed that about one-third of 62 galaxies in their sample show rotation-dominated kinematics, another one-third are dispersion-dominated objects, and the remaining galaxies are interacting or merging systems. However, more recent AO data have shown that many of these dispersion-dominated sources are in fact rotating and follow the same scaling relations as more massive galaxies (Newman et al. 2013). They also show that the ratio of rotation to random motions (V/σ) increases with stellar mass. This result shows the importance of spatial resolution for studying high-z galaxies.

While we are essentially limited by the intrinsic faintness of these objects, gravitational lensing can significantly magnify these galaxies and allow us to study their properties at a level similar to what is achieved at lower redshifts (e.g., MS 1512-cB58; see Yee et al. 1996; Pettini et al. 2000, 2002; Teplitz et al. 2000; Savaglio et al. 2002; Siana et al. 2008). Although near-IR IFU observations with AO have been able to spatially resolve high-z galaxies (Förster Schreiber et al. 2006, 2009), obtaining a resolution better than 0.2" even with AO is very difficult and lensing is the only way to obtain sub-kpc scale resolution for high-z galaxies using current instruments. Studies of this nature will truly come into their own in the future with 30m-class telescopes.

Given a sufficiently strongly lensed Lyman break galaxy (LBG), we might be able to study its dynamical state, the influence of any potential non-thermal ionizing source, such as a faint active galactic nucleus (AGN), and the physical properties of the interstellar medium.

Spatially-resolved studies of six strongly lensed star-forming galaxies at $z \sim 1.7-3.1$ using the Keck laser guide star AO system and the OSIRIS IFU spectrograph enabled Jones et al. (2010) to resolve the kinematics of these galaxies on sub-kpc scales. Four of these six galaxies display coherent velocity fields consistent with a simple rotating disk model. Using the same instrument, Jones et al. (2010) also studied spatially-resolved spectroscopy of the *Clone arc* in detail. Deriving a steep metallicity gradient for this lensed galaxy at $z = 2$, they suggested an inside-out assembly history with radial mixing and enrichment from star formation. A detailed study of the spatially-resolved kinematics for a highly amplified galaxy at $z = 4.92$ by Swinbank et al. (2009) suggests that this young galaxy is undergoing its first major epoch of mass assembly. Furthermore, analyzing near-infrared spectroscopy for a sample of 28 gravitationally-lensed star-forming galaxies in the redshift range $1.5 < z < 5$, observed mostly with the Keck II telescope, Richard et al. (2011) provided us with properties of a representative sample of low luminosity galaxies at high-z.

The small number of bright $z \sim 2$ lensed galaxies has recently been increased by a spectroscopic campaign following-up galaxy-galaxy lens candidates within the Sloan Digital Sky Survey (SDSS) (Stark et al. 2013). These high spatial and spectral resolution data, will provide us with constraints on the outflow, metallicity gradients, and stellar populations in high-z galaxies.

Given its interesting configuration and brightness, the 8 o'clock arc (Allam et al. 2007) is of major interest for the detailed investigation of the physical and kinematical properties of LBGs. Indeed, there has been a vigorous campaign to obtain a significant collection of data for this object. In particular, the following observations have been made: 5-band HST imaging covering F450W to F160W, a Keck LRIS spectrum of the rest-frame UV, near-IR H- and K-band long-slit spectroscopy with the Near InfraRed Imager and Spectrometer (NIRI) on the Gemini North 8m telescope (Finkelstein et al. 2009) and X-shooter observations with the UV-B, VIS-R and NIR spectrograph arms (Dessauges-Zavadsky et al. 2010, 2011, hereafter DZ10 and DZ11).

Measuring the differences between the redshift of stellar photospheric lines and ISM absorption lines, Finkelstein et al. (2009) suggested gas outflows on the order of 160 km s^{-1} for this galaxy. DZ10 also showed that the ISM lines are extended over a large velocity range up to $\sim$ 800 km s^{-1} relative to the systematic redshift. They showed that the peak optical depth of the ISM lines is blue-shifted relative to the stellar photospheric lines, implying gas outflows of 120 km s^{-1}.

Studying the rest frame UV, DZ10 showed that the Lyα line is dominated by a damped absorption profile with a weak emission profile redshifted relative to the ISM lines by about +690 km s^{-1} on top of the absorption profile. They suggested that this results from backscattered Lyα photons emitted in the HII region surrounded by the cold, expanding ISM shell.

DZ11 argued that the 8 o'clock arc is formed of two major parts, the main galaxy component and a smaller clump which is rotating around the main core of the galaxy and separated by 1.2 kpc in projected distance. They found that the properties of the clump resembles those of the high-z clumps studied by Swinbank et al. (2009), Jones et al. (2010), and Genzel et al. (2011). They also suggested that the fundamental relation between mass, SFR, and metallicity (Mannucci et al. 2010; Lara-López et al. 2010) may hold up to and even beyond $z = 2.5$, as also supported by two other lensed LBGs at $2.5 < z < 3.5$ studied by Richard et al. (2011).

In this work, we use near-IR IFU spectroscopy of the 8 o'clock arc with SINFONI to spatially resolve the emission line maps and the kinematics of this galaxy. In Section 2, we introduce the observed data. In this section, we also discuss the data reduction procedure and the PSF estimation as

well as the SED fitting procedure. The analysis of the IFU data is covered in Section 3. The physical properties of the 8 o'clock arc are discussed in Section 4. In Section 5, we introduce our lens modeling technique and also our source reconstruction procedure. In this section, we also present the emission line maps and the Hβ profile in the source plane. The kinematics of the galaxy are discussed in Section 6. We present our conclusions in Section 7.

2 DATA

2.1 Near-IR spectroscopy with SINFONI

We obtained J, H and K band spectroscopy of the 8 o'clock arc ($\alpha(J2000)$: 00 22 40.91 $\delta(J2000)$: 14 31 10.40) using the integral-field spectrograph SINFONI (Eisenhauer et al. 2003; Bonnet et al. 2004) on the VLT in September 2009 (Program ID: 83.A-0879 A). The observation was done in seeing-limited mode with the $0.125''$ pixel^{-1} scale, for which the total field of view (FOV) is $8'' \times 8''$. The total observing time was 4h for J, 5h for H and 3.5h for K with individual exposure times of 600s.

2.1.1 Data Reduction

The SINFONI data were not reduced with the standard ESO pipeline, but with a custom set of routines written by N. Nesvadba, which are optimized to observe faint emission lines from high-z galaxies. These routines are very well tested on SINFONI data cubes for more than 100 high-redshift galaxies, and have been used to reduce the data presented, e.g., in Lehnert et al. (2009) and Nesvadba et al. (2006a,b, 2007a,b).

The reduction package uses IRAF (Tody 1993) standard tools for the reduction of long-slit spectra, modified to meet the special requirements of integral-field spectroscopy, and is complemented by a dedicated set of IDL routines. Data are dark frame subtracted and flat-fielded. The position of each slitlet is measured from a set of standard SINFONI calibration data which measure the position of an artificial point source. Rectification along the spectral dimension and wavelength calibration are done before night sky subtraction to account for some spectral flexure between the frames. Curvature is measured and removed using an arc lamp, before shifting the spectra to an absolute (vacuum) wavelength scale with reference to the OH lines in the data. To account for the variation of sky emission, we masked the source in all frames and normalized the sky frames to the average of empty regions in the object frame separately for each wavelength before sky subtraction. We corrected for residuals of the background subtraction and uncertainties in the flux calibration by subsequently subtracting the (empty sky) background separately from each wavelength plane.

The three-dimensional data are then reconstructed and spatially aligned using the telescope offsets as recorded in the header within the same sequence of 6 dithered exposures (about one hour of exposure), and by cross-correlating the line images from the combined data in each sequence, to eliminate relative offsets between different sequences. A correction for telluric absorption is applied to each individual cube before the cube combination. Flux calibration is carried out using standard star observations taken every hour at a position and air mass similar to those of the source.

2.2 HST Imaging

Optical and NIR imaging data of the 8 o'clock arc were taken with the Wide Field Planetary Camera 2 (WFPC2) and the Near Infrared Camera and Multi-Object Spectrometer (NICMOS) instruments on the Hubble Space Telescope (Proposal No. 11167, PI: Sahar Allam). The 8 o'clock arc is clearly resolved, and was observed in the five filters WFPC2/F450W, WFPC2/F606W, WFPC2/F814W, NIC2/F110W, and NIC2/F160W, which we will refer to as B, V, I, J and H in the following. Total exposure times of 4×1100 s per BVI band, 5120 s in the J band, and 4×1280 s in the H band were obtained. The BVI frames, with a pixel scale of $0.1''$, were arranged in a four-point dither pattern, with random dithered offsets between individual exposures of $1''$ in right ascension and declination. The JH frames, with a pixel scale of $0.075''$, were also arranged in a four-point dither pattern, but with offsets between individual exposures of $2.5''$. In order to resolve the 8 o'clock arc better, the HST images were drizzled to obtain a pixel scale of $0.05''$. Figure 1 shows the B band HST image of the 8 o'clock arc and defines the images A1 through A4 as indicated. We performed photometry using the Graphical Astronomy and Image Analysis Tools (GAIA[1]). Table 1 summarises the HST photometry of the images A1-A4.

As an illustration of the power of the multi-wavelength HST data set, we show the I-H (rest frame $NUV - B$) color image of the arc in Figure 2. To construct this we convolved the WFPC2/F814W image to the same PSF as the NICMOS/F160W band before creating the color image. We can see that the substructures of the arc are better resolved in this image; for instance, we can resolve two individual images of the same clump that lie between the A3 and A2 images (see the de-lensed image of the clump shown by a purple dashed ellipse in Figure 13).

2.3 PSF Estimation

We created model PSFs for the HST images using the TinyTim package [2] (Krist et al. 2011). A measure of the PSF was also obtained using a star in the field. This estimate is consistent with TinyTim PSFs; however, because the star is significantly offset from the arc, in the rest of the paper we use only the the TinyTim PSFs when analyzing the HST data.

For the SINFONI data we use the standard star observations to estimate the PSF. The standard star was observed at the end of each Observing Block (OB) at a air mass similar to that of the data, in a fairly similar direction, and with the same setup. We integrate the standard star cubes in each band along the spectral axis to obtain the 2-dimensional images of the star.

We measure the FWHM size of the star along the x

[1] http://astro.dur.ac.uk/%7Epdraper/gaia/gaia.html
[2] http://tinytim.stsci.edu/cgi-bin/tinytimweb.cgi

Filter	Band	A1 AB magnitude	A2 AB magnitude	A3 AB magnitude	A4 AB magnitude
F450W	B	21.89 ± 1.61	21.76 ± 1.55	21.02 ± 1.07	22.65 ± 1.27
F814W	I	20.98 ± 1.03	21.06 ± 1.07	20.17 ± 0.7	21.71 ± 1.44
F160W	H	19.35 ± 0.53	19.23 ± 0.5	18.46 ± 0.34	20.35 ± 0.79

Table 1. HST photometry of the 8 o'clock arc images A1-A4. The AB magnitudes correspond to the total photometry of all components in each image.

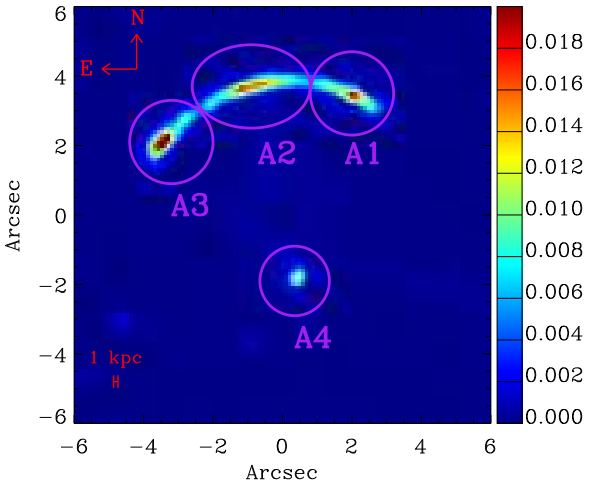

Figure 1. The B band *HST* image (in counts per second) of the 8 o'clock arc is shown. Three images A1-A3 form an arc and A4 is the counter image. The foreground galaxy (lens) has been removed from this image. The scale-bar in this and all following images are at the redshift of the source.

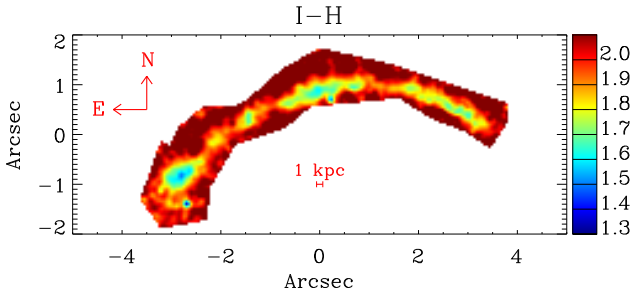

Figure 2. The $I - H$ (rest frame $NUV - B$) color image of the arc is shown. We can see that the substructures of the arc are better resolved in this image; for instance, we can resolve better two lensed images of the same clump lying between the A3 and A2 images (see Figure 13, which marks the de-lensed image of this clump with a purple ellipse). We can also resolve two images of another clump which are between the A2 and A1 images (see Figure 13, which notes the de-lensed image of this clump by a red ellipse).

and y axes of the SINFONI field-of-view by fitting a 2-dimensional Gaussian to the resulting image. We then average the individual measurements of the standard star images in each direction to determine the PSF for the corresponding band. The spatial resolutions in right ascension and declination are always somewhat different for SINFONI data due to the different projected size of a slitlet (0.25″) and a pixel (0.125″). The PSFs in the J, H and K bands are [0.99″,0.7″], [0.8″,0.66″], [0.69″,0.51″], respectively.

3 ANALYSIS OF THE SINFONI DATA

3.1 Nebular emission lines

The spectrum is first analysed using the `platefit` pipeline, initially developed for the analysis of SDSS spectra (Tremonti et al 2004, Brinchmann et al. 2004, 2008) and subsequently modified for high-z galaxies (e.g. Lamareille et al. 2006). The nebular emission lines identified in the 8 o'clock arc images A2-A3 are summarized in Table 3 . Specifically, the emission lines that we can detect in the spectra of the galaxy are [O II] $\lambda 3727, 29$, Hδ, Hγ, He II $\lambda 4686$ and Hβ. Hβ is the strongest detected emission line. In the following, we therefore concentrate on this line to further study the dynamical properties of the galaxy.

Due to the redshift of the 8 o'clock arc, we can not study the [O III] $\lambda 4959, 5007$, Hα and [N II] $\lambda 6548, 6584$ emission lines because they fall outside of the spectral range of the SINFONI bands. This means that we can not place strong constraints on the ionisation parameter or the metallicity of the galaxy using the IFU data.

3.2 The integrated Hβ profile

The Balmer lines show asymmetric profiles, especially Hβ, as was also observed by DZ11. We therefore start with a look at the integrated Hβ profile. This offers us, among other things, the possibility of testing our reduction techniques because in the absence of significant small-scale structure, profiles are expected to be similar in shape in the different sub-images. We focus here on the spectra of the highest magnification images, A2 and A3 (see Figure 1), and we only integrate over the main galaxy structure, excluding the clump identified by DZ11. The counter image (A4) is complete but is not resolved; the A1 image is only partially resolved and is located near the edge of the data cube. Figure 3 shows the integrated Hβ profiles for the images A2 and A3, respectively. We can see that the two images show the same profile, which is what one expects as they are two images of the same galaxy. This result differs from that of DZ11, who found different profiles using their long-slit data. They suggested that this might be either due to the slit orientation not optimally covering the lensed image A3, or alternatively, due to the presence of substructure perturbing the surface brightness of the A2 image. Since the IFU data show the

same profile for both images, we can rule out the possibility that substructure might have caused the differences.

We can see that the integrated Hβ profiles of both images show one main component with a broad blue wing; thus, the full profile requires a second Gaussian to be well fitted. The width of the Gaussian components for both images is 1.7 ± 0.7 Å, which gives a velocity dispersion of 104 ± 42 km s^{-1}. The velocity offset between the two fitted Gaussian components which are shown by the red dashed curves is 278 ± 63.5 km s^{-1} for the A3 image and 191 ± 63 km s^{-1} for the A2 image which are consistent within the errors. We can clearly see this blue-shifted component in both images in Figure 5 and Figure 6. DZ11 fitted two individual Gaussians to the main component of the galaxy and concluded that these fits are related to the two components (main and clump) with velocity offset of $\sim 61 \pm 8$ km s^{-1}. Since we have resolved the clump using our IFU data and did not include it when integrating the Hβ profile in Figure 3, the spectra of the A2 and A3 images plotted in Figure 3 do not contain any contribution from the clump. To illustrate the Hβ profile of the clump, we add the spectra of the two images of the clump and show the total profile with an orange line in both panels in Figure 3. We measure a velocity offset of 126 ± 42 km s^{-1} between the clump and the main component of the galaxy. The second component seen for both images (the left Gaussian fits in Figure 3) is coming from the part of the arc that was not covered by the slit used by DZ11. From the lens modeling described in Section 5, we know that the spatially separated blue-shifted component in the A2 image is coming from the north-east part of the galaxy (see Figure 13). However, we see from Figure 6 that this blue-shifted component of the A3 image is not separated spatially from the main component of the galaxy. The difference between the two images might be due to the fact that the data have insufficient spatial resolution to resolve the components in the A3 image.

3.3 Spatially-resolved emission-line properties of the 8 o'clock arc in the image plane

As we saw above, the integrated Hβ profile is not well fitted by a single Gaussian, and this is also true for Hγ and can also be seen in individual spatial pixels (spaxels) for Hβ. We therefore fit these lines with two or three Gaussian components when necessary. We carry out these fits to the Balmer lines using the MPFIT package in IDL[3]. During the fitting, we require the lines to have the same velocity widths. This could be an incorrect approximation in detail but it leads to good fits to the line profiles; the S/N and spectral resolution of the data are not sufficient to leave the widths freely variable. The spatially-resolved Hβ profiles generally show a main component, which we place at a systemic redshift of 2.7363 ± 0.0004 (rest-frame wavelength, $\lambda_{air} = 4861.325$) and an additional component that is blue-shifted relative to the main component by 120-300 km s^{-1}. The best-fit Gaussian intensity map of these blue-shifted and main components of the galaxy are shown in Appendix A for the A2 and A3 images. There is also a redshifted component that is detectable close to the clumps between the A3 and A2 images (see Figure 1). This component is spatially separated from the main component by 1″ (mentioned also by DZ11). The velocity difference between this component and the main component is ~ 120 km s^{-1}.

The central map in Figure 4 shows the spatial distribution of Hβ line flux across the main components of the arc, where we have integrated the line flux between $\lambda = 4855$Å and 4867Å. The small panels around the Hβ line map show the Hβ profiles of different spatial pixels as indicated. These individual panels clearly show that the Hβ line shows different profiles in different regions across the lensed images.

We can show these components in an alternative way, using the position-velocity diagrams in Figure 5 and Figure 6 for the A2 and A3 images, respectively. Figure 5 clearly shows two spatially separated components corresponding to the A2 image. The peak of one component is blue-shifted by $\sim$130 km s^{-1} and spatially separated by $\sim$ 1″ relative to the peak of the other. DZ11 identified these two components with the main galaxy and the clump because they could not separate the clump from the rest of the galaxy using long-slit observations. Here, using IFU data, we have excluded the clump from these position-velocity diagrams. The two retained components are associated with the galaxy and the red (in the spectral direction) component that DZ11 identified as the clump is part of the main galaxy. From the lens modeling that we describe in Section 5, we will see that the blue-shifted component comes from the eastern part of the galaxy (see Figure 13). The A3 image in Figure 6 also shows this blue-shifted component but not as spatially separated. We will argue below (see Section 6.3) that a reasonable interpretation of this component is that it corresponds to an outflow from the galaxy.

4 THE PHYSICAL PROPERTIES OF THE 8 O'CLOCK ARC

4.1 SED fitting

To determine the physical parameters of the 8 o'clock arc, we fit a large grid of stochastic models to the *HST* *BVIJH* photometry to constrain the spectral energy distribution (SED). The grid contains pre-calculated spectra for a set of 100,000 different star formation histories using the Bruzual & Charlot (2003, BC03) population synthesis models, following the precepts of Gallazzi et al. (2005, 2008). Figure 7 shows the best-fit SED. We corrected the observed magnitudes for galactic reddening. We corrected the photometry for Galactic foreground dust extinction using $E(B-V)_{Gal} = 0.056$ (Schlegel et al. 1998).

We follow the Bayesian approach presented by Kauffmann et al. (2003) to calculate the likelihood of the physical parameters. We take the median values of the Probability Distribution Functions (PDFs) as our best estimated values. In particular, the parameters we extract are the stellar mass, $M_\star$, the current star-formation rate, SFR_{SED}, the dust attenuation, τ_V and the r-band luminosity weighted age. The physical parameters from the SED fitting are summarised in Table 2.

DZ11 also carried out SED fitting to the photometric data for the 8 o'clock arc. They explored cases with

[3] http://cow.physics.wisc.edu/∼craigm/idl/mpfittut.html

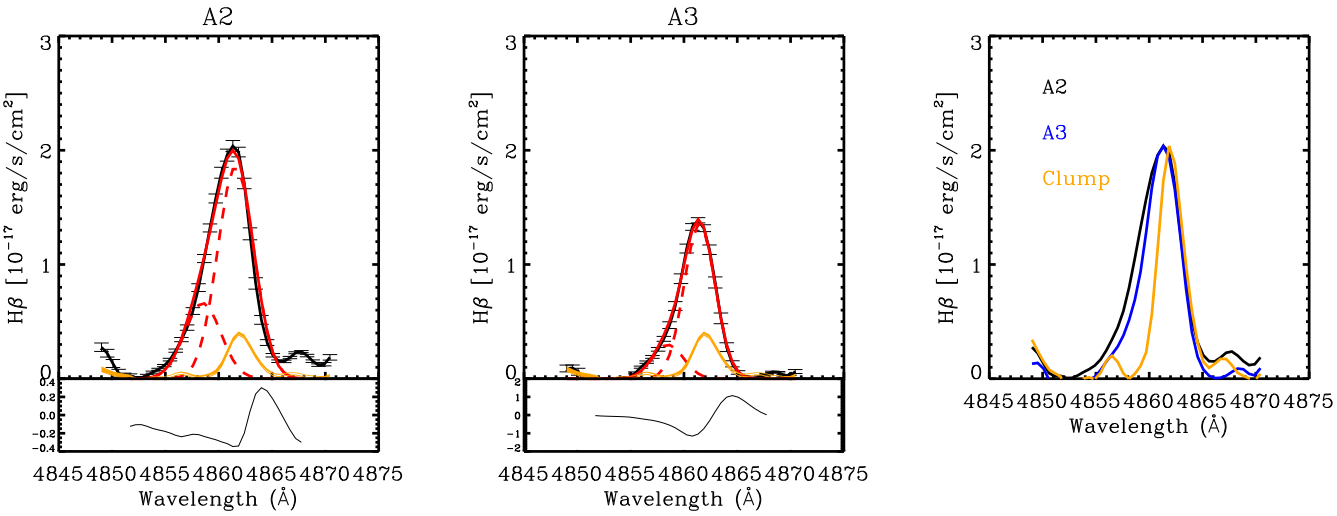

Figure 3. Left: integrated Hβ profile of A2, the highest magnification image, showing two components that we can also resolve in individual spaxels. Middle: integrated Hβ profile of the A3 image. Both images show the same Hβ profile (see right panel). The widths of the Gaussian components for both images (red dashed lines) are 1.7 Å, which gives velocity dispersions of 104 km s^{-1}. The velocity offset between the two fitted Gaussian components is 278 km s^{-1} for the A3 image and 191 km s^{-1} for the A2 image. To illustrate the Hβ profile of the clump, we add the spectra of two images of the clump and show this profile in orange in both panels (note that the A2 and A3 profiles shown in this figure do not contain the clump profile). The velocity offset between the clump Hβ profile and the main galaxy Hβ profile is 126 km s^{-1}. The bottom panels show the residuals if we fit the Hβ profile of each image with a single Gaussian. Right: Hβ profiles of the A2 and A3 images and the clump are shown; the profiles are normalised to have the same peak.

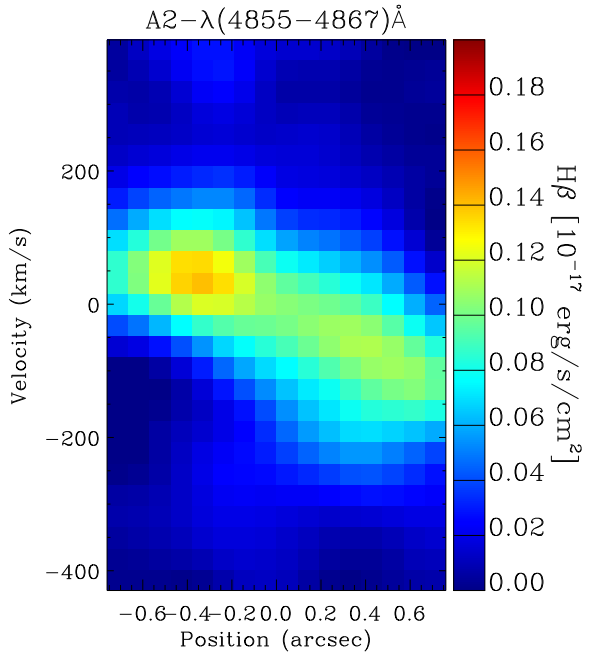

Figure 5. Position-velocity diagram of the A2 image, with negative values corresponding to blue shift. There are two components that are clearly offset both spatially and in the velocity direction. The velocity offset between the two components is $\sim$ 130 km s^{-1}, and the spatial separation between them is $\sim 1''$. Position is relative to the center of the A2 image along the length of the arc.

and without nebular emission (Schaerer & de Barros 2009, 2010). Since their results do not change significantly, we do not consider the effect of nebular emission in our study. They also included photometry from IRAC, which in principle should improve constraints on stellar masses. We have opted against using these data, keeping the higher spatial resolution of *HST* + SINFONI, as the stellar mass from our fits is only slightly higher, but consistent with their results within the errors, and this is the quantity of most interest to this paper.

To compare our SED fit to the observed continuum spectrum, we estimate the continuum in the SINFONI spectra by taking the median of the spectrum in bins of 10 Å. Figure 8 shows the *H*-band median continuum, summed over all images in the arc, in comparison to the estimated model continuum from the SED fitting. The agreement is satisfactory, although the S/N of the continuum precludes a detailed comparison.

4.2 Parameters derived from emission line modeling

To derive physical parameters for the ionised gas in the 8 o'clock arc, we make use of a grid of Charlot & Longhetti (2001, hereafter CL01) models. We adopt a constant star formation history (SFH) and adopt the same grid used by Brinchmann et al. (2004, hereafter B04; see Appendix A in Shirazi & Brinchmann (2012) and B04 for further details). In total, the model grid used for the fits has 2×10^5 different models. The model grids and corresponding model parameters are summarised in Table 4. Our goal here is to

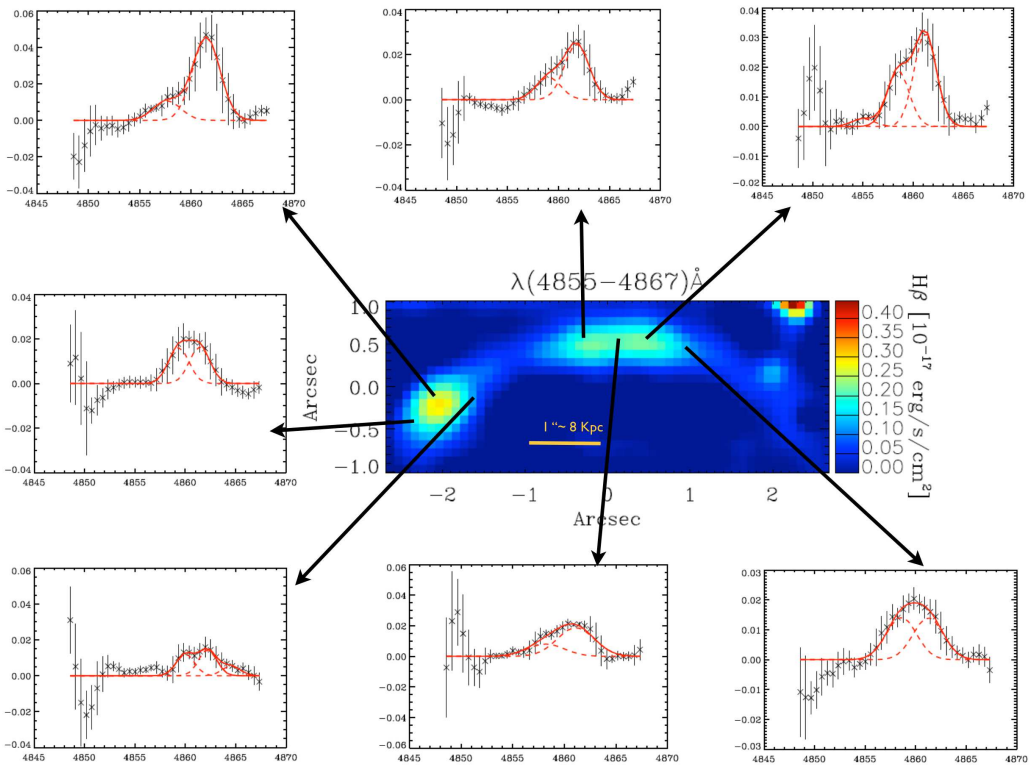

Figure 4. Middle panel shows Hβ line map of the arc. Small panels around the Hβ line map show the Hβ profiles of different spatial pixels as indicated. The Hβ line map was integrated over 4855Å< $\lambda_{\rm rest}$ <4867Å. We can see that Hβ shows different profiles at different pixels, which are composed of multiple components.

Image	log $(M_\star/M_\odot)$	log$(SFR/M_\odot\ yr^{-1})$	log$(sSFR/yr^{-1})$	log(age/yr)	τ_V	log$(Z/Z_\odot)$
A2	$10.24^{9.99}_{10.69}$	$1.86^{1.71}_{1.96}$	$-8.47^{-8.98}_{-8.17}$	$8.32^{7.68}_{8.93}$	$0.17^{0.07}_{0.3}$	$0.08^{-0.19}_{0.2}$
A3	$10.32^{10.08}_{10.77}$	$1.96^{1.82}_{2.07}$	$-8.44^{-8.93}_{-8.15}$	$8.28^{7.67}_{8.90}$	$0.17^{0.07}_{0.3}$	$0.07^{-0.2}_{0.2}$

Table 2. Physical parameters derived from SED fitting. Parameters from left to right are stellar mass, $M_\star$, current star-formation rate, SFR, specific star formation rate (sSFR), r-band luminosity weighted age, dust attenuation τ_V and metallicity.

derive representative overall parameters for the galaxy, and since the fitting methodology outlined in B04 works best with [O II] λ3727, Hβ, [O III] λ4959, Hα, and [N II] λ6584 all available, we here take the emission line measurements from DZ11 since the last three lines fall outside the spectral range of our SINFONI data cube. For the quantities that only depend on line ratios, i.e., all but the star formation rates, this is appropriate, but for the star formation rate we need to correct for light missed by the long slit observations of DZ11, and we do this by normalising to the Hβ line flux from the SINFONI data.

We use the same Bayesian methodology as for the SED fit and again take the median value of each PDF to be the best estimate of a given parameter and the associated ±1 σ confidence interval to be spanned by the 16th–84th percentiles of the PDF.

In Figure 9 we illustrate our technique by showing the effect on the PDFs of parameters, when we fit a model to an increasing number of the emission lines. We start with [O II] λ3727 and show how we get more well defined PDFs for the indicated parameters as we add the emission lines indicated on the left. We show the PDFs for the dust optical depth in V-band, the gas phase oxygen abundance, the ionisation parameter, the conversion factor from Hα luminosity to star formation rate (see CL01 for further details), the gas mass surface density, the dust-to-gas ratio and the metal-to-dust ratio of the ionised gas. The latter three quantities are discussed in some detail in Brinchmann et al. (2013, here-

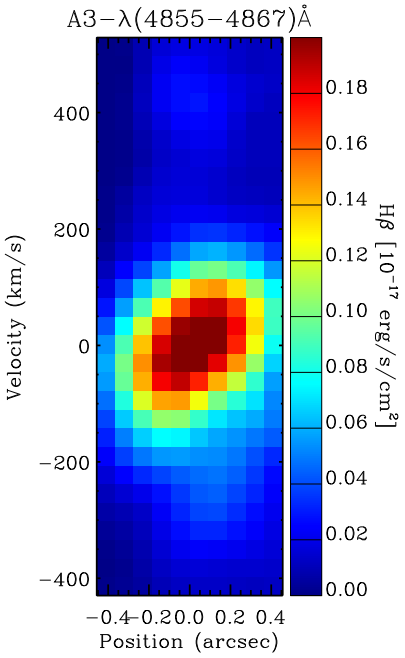

Figure 6. Position-velocity diagram of the A3 image. This image shows a blue-shifted component that is not spatially separated, in contrast to Fig. 5. Position is relative to the center of the A3 image along the length of the arc.

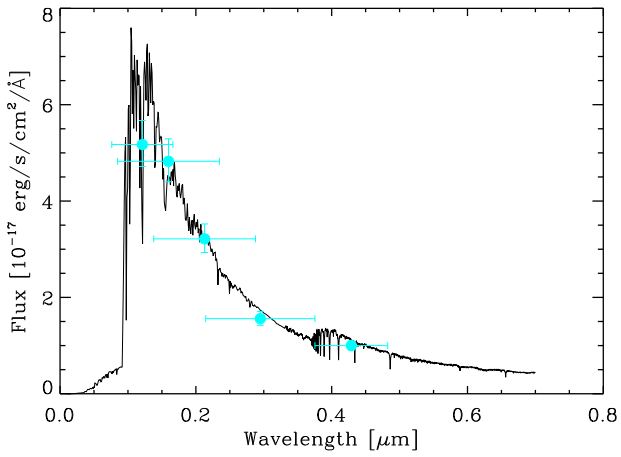

Figure 7. *HST* photometry for the 8 o'clock arc in the rest-frame (cyan filled circles) with the best-fit SED (solid curve) over plotted. The horizontal error bars show the wavelength coverage of the *HST* filters.

after B13) and we discuss them in more detail below. The resulting PDFs are shown for the A3 image and the best-fit parameters derived from the final PDFs are summarised in Table 5.

The oxygen abundance reported by DZ10 and DZ11 is lower that what we find. This is not entirely surprising for two reasons. First, it is well-known (e.g. Kewley & Ellison 2008) that metal abundance estimators show significant offsets, so even when converted to a solar scale, one has to accept a systematic uncertainty in any comparisons that use

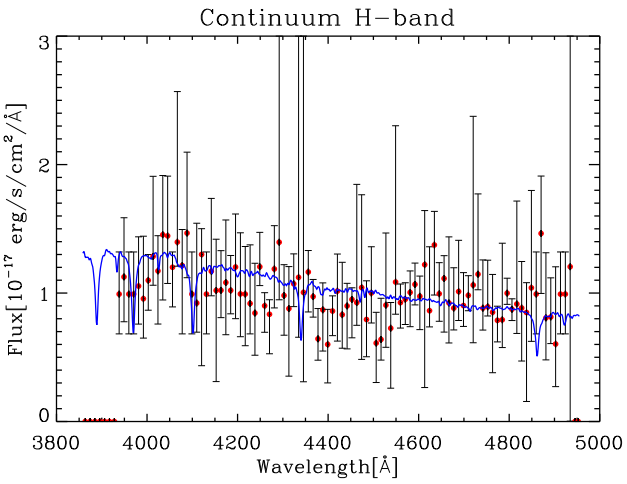

Figure 8. Median continuum in the H-band calculated in bins of 10Å (red filled circles). Error bars show 16th and 84th percentiles of the distribution around the median. Estimated model continuum from SED fitting is shown by the blue solid curve.

different methods for metallicity estimates. Second, the estimates in DZ10 and DZ11 primarily rely on the calibration relationships (N2 calibration) from Pettini & Pagel (2004), which are based on local HII regions and an extrapolation to higher metallicity. The use of these calibrated relationships implicitly assumes that the relationship between ionisation parameter and metallicity is the same at high and low redshifts. This is a questionable assumption; indeed the electron density we find for the 8 o'clock arc is considerably higher than seen on similar scales in similar galaxies at low redshift (see Figure 10), indicating that the U-Z relationship is different at high redshift, and thus that the N2 calibration is problematic. In our modeling we leave U and Z as free variables; thus, we are not limited by this. It is difficult to ascertain which approach is better but the advantage of our approach for the 8 o'clock arc is that it uses exactly the same models which used to fit local SDSS samples.

It is well-known that the estimation of ISM parameters from strong emission lines is subject to systematic uncertainties (see however B13 for an updated discussion). To reduce the effect of these uncertainties, we have also assembled a comparison sample of star-forming galaxies at $z \sim 0.1$ from the SDSS. We used the MPA-JHU value added catalogues (B04, Tremonti et al. (2004)) for SDSS DR7[4] as our parent sample. We define a star-forming galaxy sample on the basis of the [N II] 6584/Hα versus [O III] 5007/Hβ diagnostic diagram, often referred to as the BPT diagram (Baldwin, Phillips & Terlevich 1981). For this we used the procedure detailed in B04 with the adjustments of the line flux uncertainties given in B13. From this parent sample, we selecte all galaxies that have stellar mass within 0.3 dex of the value determined for the 8 o'clock arc and whose star formation rate is within 0.5 dex of the 8 o'clock arc, based on the parameters determined from SED fitting to the A2 image (Table 2). This resulted in a final sample of 329 galaxies, which we compare to the 8 o'clock arc below.

[4] `http://www.mpa-garching.mpg.de/SDSS/DR7`

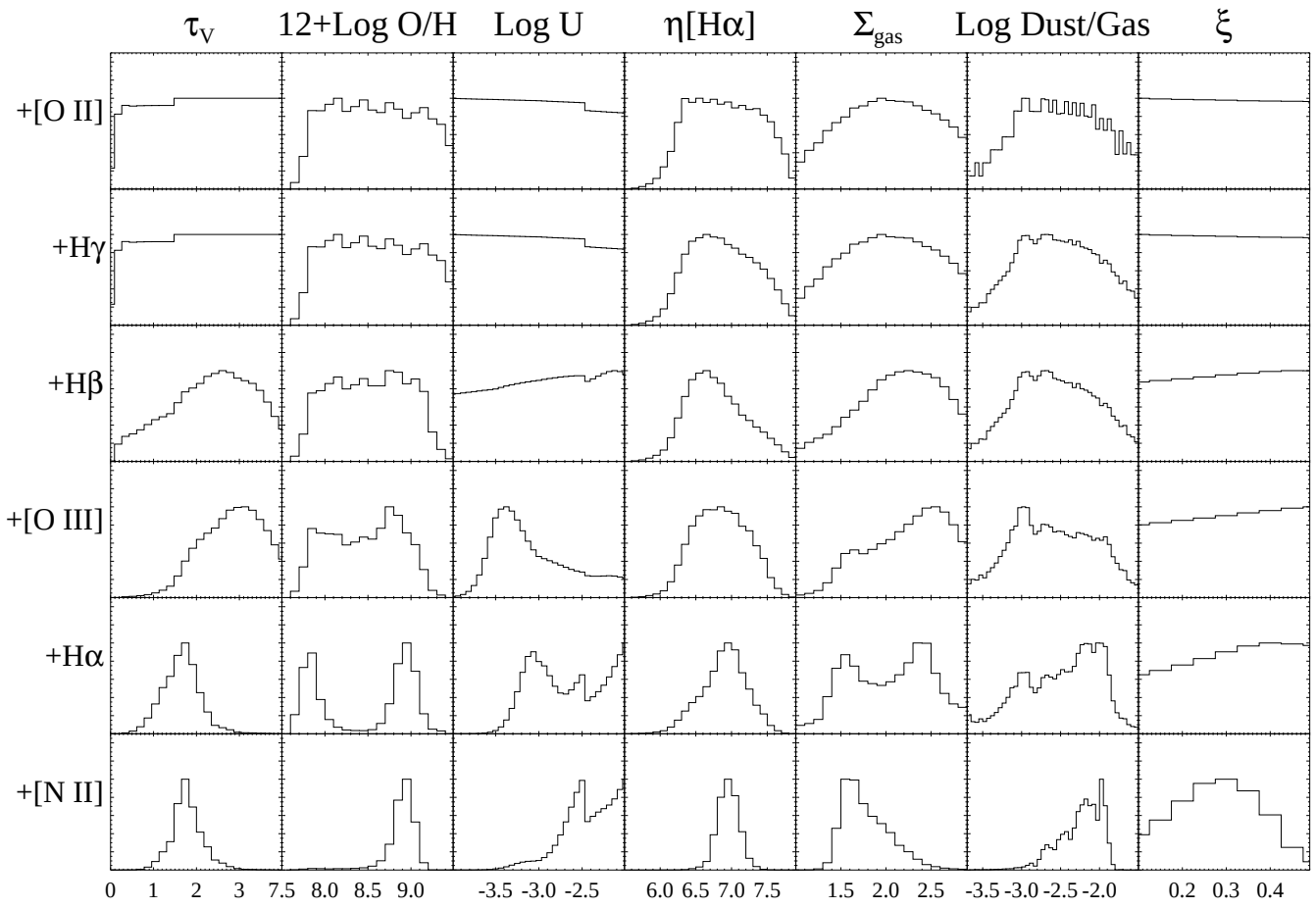

Figure 9. The PDFs for optical depth in the V-band, the gas phase oxygen abundance, the logarithm of the ionization parameter, $\log_{10}$ of the conversion factor from observed Hα luminosity to star formation rate, the logarithm of the gas surface density in $M_{\odot}/\mathrm{pc}^2$, the log of the dust-to-gas ratio and the metal-to-gas ratio. From one row to the next we include the line indicated on the left side in the fitting in addition to the previous emission lines. For the observational data in this figure we make use of emission line fluxes measured by DZ11, from their Table 2, for image A3 (see Figure 1). Our best-fit parameters and the associated 16th-84th percentiles are summarized in Table 5. The abundance of oxygen reported by DZ11 is lower than what we find.

Line	λ_{air} (Å)	A2	A3
[O II]	3726.032	65.8 ± 1.9	36.2 ± 1.6
[O II]	3728.815	58.2 ± 1.8	29.8 ± 1.5
Hδ	4101.734	25.6 ± 0.6	12.9 ± 0.3
Hγ	4340.464	45.3 ± 0.6	26.3 ± 0.3
Hβ	4861.325	102.6 ± 1.4	75.8 ± 1

Table 3. Nebular emission lines identified in the 8 o'clock arc images A2 and A3 and their fluxes. Fluxes are not corrected for lens magnification. Integrated line fluxes are in units of $10^{-17}\mathrm{erg\,s^{-1}cm^{-2}}$.

Parameter	Range
Z, metallicity	$-1 < \log(\mathrm{Z/Z_{\odot}}) < 0.6$, 24 steps
U, ionization parameter	$-4.0 < \log \mathrm{U} < -2.0$, 33 steps
τ_V, total dust attenuation	$0.01 < \tau_V < 4.0$, 24 steps
ξ, dust-to-metal ratio	$0.1 < \xi < 0.5$, 9 steps

Table 4. The CL01 model grid used in the present work.

4.3 AGN contribution

The preceding modeling assumes that the ionizing radiation in the 8 o'clock arc is dominated by stellar sources. The position of the 8 o'clock arc in the BPT diagnostic diagram (see Figure 6 in Finkelstein et al. 2009), which has been widely used for classifying galaxies, does, however suggest that the emission lines from this galaxy might be contaminated by an AGN. However, there is some evidence indicating that the AGN contribution for this galaxy is negligible.

First, high-resolution VLA imaging at 1.4 and 5 GHz show that, although there is a radio-loud AGN associated with the lensing galaxy and the arc is partially covered by the radio-jet from this AGN, there is no detectable radio emission from the unobscured region of the arc down to a

	16th[a]	median [b]	84th [c]
$\log(Z/Z_\odot)$[d]	0.046	0.130	0.196
log U[e]	-2.6	-2.2	...[f]
τ_V[g]	1.1	1.6	1.8
SFR $(M_\odot\ yr^{-1})$[h]	157	165	173
$\log(\Sigma_{\rm gas}/M_\odot\ pc^{-2})$[i]	1.46	1.60	1.87
12+Log O/H	8.86	8.93	9.02

[a] The 16$^{\rm th}$ percentile of the PDF of the given quantity.
[b] The 50$^{\rm th}$ percentile, or median, of the PDF of the given quantity.
[c] The 84$^{\rm th}$ percentile of the PDF of the given quantity.
[d] The log of the total gas-phase metallicity relative to solar.
[e] The log of the ionization parameter evaluated at the edge of the Strömgren sphere (see CL01 for details).
[f] The electron density in the 8 o'clock arc is higher than that assumed in the CL01 models, and the ionization parameter is therefore close to the edge of the model grid, to we do not quote an upper limit.
[g] The dust attenuation in the V-band assuming an attenuation law $\tau(\lambda) \propto \lambda^{-1.3}$.
[h] The star formation rate.
[i] The log of the total gas mass surface density.

Table 5. Physical parameters of the ISM derived from spectrum of the A3 image.

3σ flux-density limit of 108 μJy beam^{-1} (Volino et al. 2010). Second, we can detect He II λ4686 for this galaxy, a high-ionization line that is very sensitive to the AGN contribution. Therefore, we can use this line as a probe to estimate the AGN contribution to the spectrum of this galaxy. We use a new diagnostic digram of He II /Hβ versus [N II] /Hα introduced by Shirazi & Brinchmann (2012) to calculate this. As we do not have [N II] and Hα from the SINFONI observation, we use the DZ11 estimates for these emission lines. The He II λ4686/Hβ is not very sensitive to electron temperature and metallicity. Therefore using the DZ11 estimate for [N II] /Hα is sufficient for us to locate the position of this galaxy in the He II /Hβ diagram. Shirazi & Brinchmann (2012) derive an almost constant line vs. metallicity at which the contribution of an AGN to the He II emission amounts to about 10%. They showed if the He II is contaminated by this amount, the total AGN contribution to other emission lines in the spectrum of the galaxy is less than 1% (see Figure 3 in Shirazi & Brinchmann 2012). As the position of the 8 o'clock arc in this digram (log He II /H$\beta = -1.4$) is below the above mentioned line, we can conclude that the contribution of AGN to the optical emissions is negligible.

We note that the broad He II λ1640 emission found by DZ10 can be affiliated to the presence of Wolf-Rayet stars (see also Eldridge & Stanway 2012).

4.4 Star formation rate and dust extinction

We have two main methods available to determine the star formation rate of the 8 o'clock arc from its emission line properties. We can use the SFR derived from the emission line fits described above, but to provide spatially resolved SFR maps we need to turn to the lines available in the SINFONI data cube. The H$\alpha\lambda$6563 emission line is commonly used as a star formation rate indicator at low redshift (Kennicutt 1998). Unfortunately, for the redshift of the 8 o'clock arc, Hα falls outside of the spectral range of the K band of SINFONI, and we can not use this indicator to derive the spatially resolved SFR. We are therefore limited to using H$\beta\lambda$4861 as a tracer of the spatially resolved SFR. The advantages and disadvantages of using this indicator to measure the SFR were originally discussed by Kennicutt (1992) and were studied in detail by Moustakas et al. (2006). In comparison to Hα, Hβ is more affected by interstellar dust and is more sensitive to the underlying stellar absorption (see Section 3.3 and Figure 7 in Moustakas et al. 2006).

We use the empirical SFR calibrations from Moustakas et al. (2006, Table 1), parametrized in terms of the B-band luminosity, to calculate the SFR from Hβ luminosity:

$$SFR\ (M_\odot yr^{-1}) = 10^{-0.24} \times 10^{0.943} \times 10^{-42} \frac{\rm L(H_\beta)}{erg\ s^{-1}}. \quad (1)$$

Moustakas et al. (2006) derived the SFR calibration assuming a Salpeter initial mass function (IMF, Salpeter 1955) over 0.1-100 $M_\odot$. The correction factor of $10^{-0.24}$ in Equation (1) is used to correct to a Chabrier IMF (Chabrier 2003). We interpolate between bins of L(B) to obtain the relevant conversion factor from Hβ luminosity to SFR.

We use a dust extinction $E(B-V) = 0.3 \pm 0.1$ derived from the Hγ/Hβ Balmer line ratio with an intrinsic Hγ/Hβ = 0.468 to correct both SFRs for dust extinction. This is consistent with the estimate of DZ11 within the errors. We used magnification factors of $\mu^{\rm A2} = 6.3$ and $\mu^{\rm A3} = 4.9$ to correct the SFR estimates for the effect of gravitational lensing. The magnification calculated using the lens modeling described in Section 5. We use 0.012 contour level (in count per second unit) in the $B\ HST$ image for detecting individual images.

We measure H$\beta = (102.6 \pm 1.4) \times 10^{-17}$ erg s^{-1}cm^{-2} for the A2 image corresponding to an observed SFR of 228 ± 10.9 $M_\odot\ yr^{-1}$ and H$\beta = (75.8 \pm 1.) \times 10^{-17}$ erg s^{-1}cm^{-2} for the A3 image, corresponding to an observed SFR of 227 ± 10.5 $M_\odot\ yr^{-1}$(corrected for gravitational lensing magnification and dust extinction).

We can contrast this result to the integrated SFRs derived for the A2 and A3 images by fitting the CL01 models, after scaling the DZ11 line fluxes to match the Hβ flux from the SINFONI cube. These are 160 ± 12 $M_\odot\ yr^{-1}$ and 165 ± 10.5 $M_\odot\ yr^{-1}$, respectively. These values are somewhat discrepant but we note that systematic uncertainties are not taken into account in the calculation here.

More importantly, the Hβ calibration allows us to calculate maps of the spatial distribution of the optically visible star formation in the 8 o'clock arc. Furthermore, we can make use of our decomposition of the Hβ profile to calculate maps for each component. This is shown in Figure 11 which shows these three calculated SFR maps for the A2 image. These were derived by integrating over the blue ($\lambda(4855-4859)$Å), green ($\lambda(4859-4863)$Å), and red ($\lambda(4863-4867)$Å) parts of the Hβ profile. We can see that the blue and red maps peak at different part of the image, which suggests that they represent different components of the galaxy.

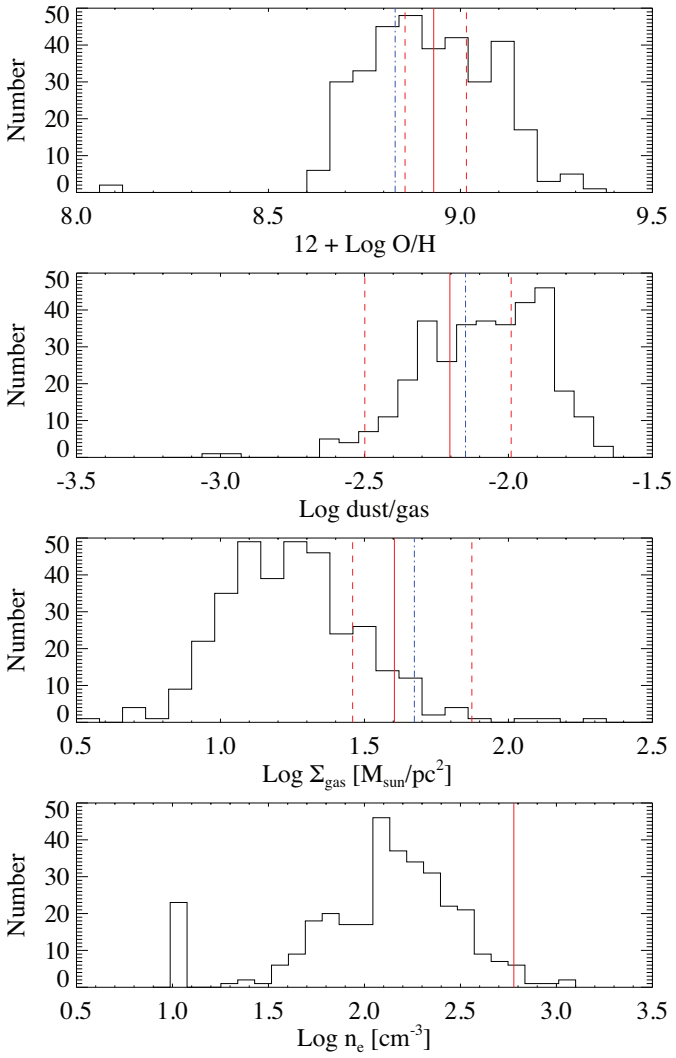

Figure 10. Top panel: distribution of oxygen abundance for the local comparison sample. The solid red line shows the median value derived for image A3 with the dashed vertical lines showing the 16% and 84% percentiles. The dash-dotted line shows the median estimate for image A2 and is consistent with that derived for A3. Second panel: same for the dust-to-gas ratio. Third panel: same for gas surface mass density. Bottom panel: distribution of electron densities in the comparison sample. These were derived using the ratio of the [S II] 6716,6731 lines assuming an electron temperature of $T_e = 10^4$ K. The estimated electron density for the 8 o'clock arc, derived from the ratio of the [O II] 3726,3729 lines, is shown by the solid red line.

4.5 Metallicity and dust-to-gas ratio

The modeling described above gives an estimate of the oxygen abundance and the dust-to-gas ratio of the 8 o'clock arc. Our best-fit oxygen abundance, $12 + \log \mathrm{O/H} = 8.93^{+0.09}_{-0.07}$ (random errors only), is consistent with the determination by DZ11 within the error. In the top panel of Figure 10 we compare this value to that determined for our local comparison sample. The values for A3 are shown as the solid red lines, with the 1σ confidence interval indicated by the dashed red lines. We also calculate values from the fluxes provided for image A2, and these are shown as the dot-dashed blue lines. We suppress the uncertainty estimate for this latter estimate but it is similar to that of A3; thus, the two measurements are consistent given the error bars.

Two points are immediately noticeable from this plot. First, the oxygen abundance is mildly super-solar, (the solar oxygen abundance in the CL01 models is 8.82), and second, the value for the 8 o'clock arc is the same as for the local comparison sample. Since the local sample was selected to have approximately the same stellar mass and star formation rate as the 8 o'clock arc, we must conclude that the 8 o'clock arc lies on the stellar mass–oxygen abundance–star formation rate manifold found locally (Mannucci et al. 2010). A similar conclusion was also found by DZ11.

The second panel in Figure 10 shows the dust-to-gas ratio (DGR) of the SDSS comparison sample as a histogram and the values for the 8 o'clock arc as the vertical lines as in the top panel. The uncertainty in $\log \mathrm{DGR}$ is fairly large, but there is no evidence that the 8 o'clock arc differs significantly from similar galaxies locally. As we will see next, this does not necessarily imply that the ISM has all the same properties.

4.6 The gas surface mass density

It is of great interest to try to estimate the gas content of high redshift galaxies in general, and we have two methods to do this for the 8 o'clock arc. The first is to use the Kennicutt–Schmidt relation (Schmidt 1959; Kennicutt 1998) between the gas surface density and star formation rate per unit area to convert our spatially resolved SFRs to gas surface densities. We can then use this estimated gas surface density to calculate the gas mass. The estimated gas surface density is plotted in Figure 12 and is simply a transformation of the SFR map shown earlier. We can then integrate this surface density of gas to get an estimate of the total gas mass. With the canonical calibration of Kennicutt (1998) this gives an estimate of $\log(M_{\mathrm{gas}}/M_{\odot}) = 10.43 \pm 1.18$. If instead we use the calibration used by DZ11 (Bouché et al. 2007), we find a total gas mass of 10.30 ± 1.20. In either case, the gas content is comparable to the total stellar mass of the galaxy.

We can also estimate the gas content in a way independent of the star formation rate by exploiting a new technique presented in B13, which exploits the temperature sensitivity of emission lines to provide constraints on the dust-to-metal ratio; together with an estimate of the dust optical depth (see B13 for detail), one can derive a constraint on the surface mass density of gas (molecular plus atomic). B13 show that this technique can give gas surface densities in agreement with H I+H_2 maps to within a factor of 2. The results of our fits are shown in Fig. 9. In passing, we note that this technique, in contrast to the Kennicutt-Schmidt method, only relies on line ratios and these lines all originate in much the same regions; thus, lensing amplification should be unimportant here.

The median estimate is $\log(\Sigma_{\mathrm{gas}}/M_{\odot}\ pc^{-2}) = 1.60$, which is consistent with the value that derived using the Kennicutt-Schmidt relation but derived in an independent manner, and crucially using a method that is formally independent of the star formation rate. We contrast the estimate of $\log \Sigma_{\mathrm{gas}}$ for the 8 o'clock arc to the SDSS comparison sample in the third panel of Figure 10. The median value for the local sample is $\Sigma_{\mathrm{gas}} \approx 17\ M_{\odot}\ \mathrm{pc}^{-2}$, while the median es-

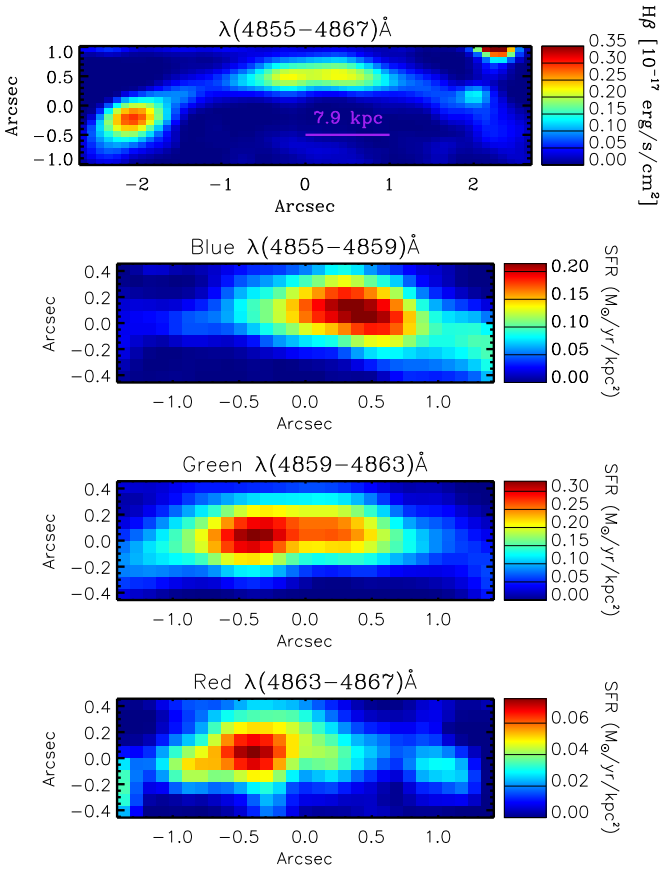

Figure 11. Top: Hβ line map of the arc. This map is not corrected for magnification. Lower panels: three different calculated SFR (corrected for lensing magnification and dust extinction) maps for the A2 (middle) image. SFRs are derived by integrating over the blue, green and red parts of the Hβ profile, respectively from top to bottom. The wavelength ranges covered in the indicated above the SFR maps. The color scale shows the SFR per kpc^2 as indicated.

timate for the 8 o'clock arc is $\Sigma_{\rm gas} \approx 40\ M_\odot\ {\rm pc}^{-2}$. Since this comparison is differential and does not depend on scaling relations calibrated on local samples, the conclusion that the surface density of gas in the 8 o'clock arc is more than twice that of similar $z \sim 0.1$ galaxies should be fairly robust. Thus, while the 8 o'clock arc does lie on the M_*–O/H–SFR relation, it has a significantly higher gas surface density than galaxies lying on the same relation locally. This highlights the fact that even though a particular scaling relation is established at high-z, it does not imply that galaxies lying on the relation are necessarily similar to local galaxies.

4.7 Electron density

We can estimate the electron density using the [O II] λ3729/[O II] λ3726 ratio. Both the X-shooter and the SINFONI observations of the 8 o'clock arc give similar ratios for the [O II] λ3729, 3726 lines. The SINFONI observations give a value of [O II] λ3729/[O II] λ3726 = 0.88 which corresponds to a high electron density of $n_e \sim 600$ cm^{-3} for this galaxy. High electron densities have been found in

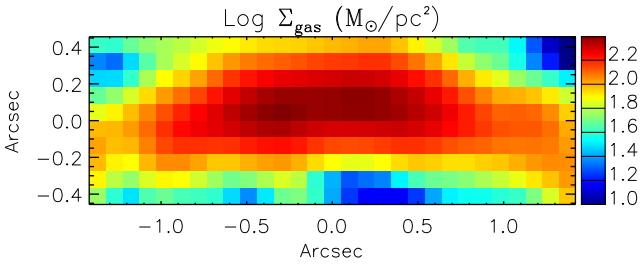

Figure 12. The resolved gas surface density for the A2 image estimated using the Kennicutt-Schmidt relation.

many other high-z galaxies (see e.g. Lehnert et al. 2009; Wuyts et al. 2012; Lehnert et al. 2013).

For the local comparison sample we are unable to reliably estimate n_e from the [O II] line ratio, so we use the [S II] 6717,6731 lines instead. These values are compared to that for the 8 o'clock arc in the bottom panel of Figure 10 and as that figure makes clear, the 8 o'clock arc has significantly higher electron density than similar SDSS galaxies. Note that the [S II] ratio is not very sensitive to electron density variations at $n_e < 100$ cm^{-3}, hence the somewhat truncated shape of the distribution there.

The high electron density is likely to lead to a high ionization parameter, and this is born out by our fits (Figure 9). Indeed, the 8 o'clock arc lies close to the maximum ionization parameter in the CL01 models, and its electron density is well above the value assumed ($n_e = 100$ cm^{-3}) in the CL01 model calculations. For this reason, we prefer to focus on the n_e determination which is independent of this and which implies a higher ionization parameter for this galaxy relative to nearby objects.

More immediately, the electron density is related to the pressure in the H II region through $P = n_e k T_e$, and since the electron temperature in the H II region almost certainly will be very similar in the low-z sample and the 8 o'clock arc, given that their metallicities are similar, we conclude that the pressure in the H II regions in the 8 o'clock arc is ~ 5 times higher than in the typical SDSS comparison galaxy.

The reason for this elevated H II region pressure is less clear. Dopita et al. (2006) showed that for expanding H II regions the ionization parameter depends on a number of parameters. A particularly strong dependence was seen with metallicity, but as our comparison sample has similar metallicity to that of the 8 o'clock arc we can ignore this. The two other major effects on the ionization parameter come from the age of the H II region and the pressure of the surrounding ISM. It is of course possible that we are seeing the 8 o'clock arc at a time when its H II regions have very young ages, and hence high ionization parameter, relative to the local comparison sample. Since we are considering very similar galaxies in terms of star formation activity and probe a fairly large scale this seems to be a fairly unlikely possibility, but it cannot be excluded for a single object. The pressure in the surrounding ISM in Dopita et al (2006) models has a fairly modest effect on the ionization parameter, $U \propto P_{\rm ISM}^{-1/5}$.

Thus, we would expect the ISM density in the 8 o'clock arc to also be higher than in the comparison sample by a

factor of ~ 5. We already saw that the gas surface density is higher than in the comparison sample by a factor > 2 thus this is not an unreasonable result and it does not seem to be an uncommon result for high-z galaxies (Shirazi et al. 2013, submitted).

5 SOURCE RECONSTRUCTION

In order to study emission line maps and the kinematics of the galaxy in the source plane, we need to reconstruct the morphology of the 8 o'clock arc using gravitational lens modeling. The lens modeling also allows us to derive the magnification factors of the multiple-lensed images which were used to estimate the corrected SFR and the stellar mass of the galaxy in the previous section. In the following, we describe our lens modeling procedure.

5.1 Gravitational lens modeling

To reconstruct the lens model for this system, we make use of the Bayesian grid based lens modeling technique presented by Vegetti & Koopmans (2009), which is optimized for pixelized source surface brightness reconstructions.

In order to obtain a robust lens model, we first consider the high resolution and high signal-to-noise ratio B band HST image. We assume the lens mass distribution to follow a power-law elliptical profile with surface mass density, in units of the critical density, defined as follows

$$k(x,y) = \frac{k_0}{2\sqrt{q}}(2-\frac{\gamma}{2})\ ((x-x_0)^2+\frac{(y-y_0)^2}{q^2}+{r_c}^2)^{(\frac{1-\gamma}{2})} \quad (2)$$

We also include a contribution from external shear. In particular, the free parameters of the model are the mass density normalization k_0, the position angle θ, the mass density slope γ ($\gamma = 2.0$ for an isothermal mass distribution), the axis ratio q, the centre coordinates x_0 and y_0, the external shear strength Γ, the external shear position angle Γ_θ, and the source regularization level (i.e., a measure of the level of smoothness of the source surface brightness distribution), while the core radius is kept fixed to the negligible value of $r_c \equiv 0$. The most probable parameters of the model are $k_0 = 3.367$, $\theta = 14.54$, $q = 0.618$, $\gamma = 2.009$, $\Gamma = 0.062$, $\Gamma_\theta = 10.597$. Using the same mass model for the lens galaxy, we also model the NICMOS data. While the B band HST data probe the rest frame UV and have a higher resolution in comparison to the NICMOS data, the latter have the advantage of providing us with information about the continuum in the J and H bands, where Hβ and [O II] emission lines are located in the spectra. The most probable mass model for the NICMOS data has the following parameter values: $k_0 = 3.328$, $\theta = 14.30$, $q = 0.672$, $\gamma = 2.020$, $\Gamma = 0.077$ $\Gamma_\theta = 13.37$. Both results are consistent with DZ11 best-fit parameters, within the error bars. However, unlike DZ11, we do not optimize for the core radius because Einstein rings only make is possible to constrain the mass distribution at the Einstein radius.

These two most probable models are used to map the image plane into the source plane and reconstruct the original morphology of the 8 o'clock arc in the B and H bands, respectively. Thanks to the Bayesian modeling technique, the most probable source surface brightness distribution for a given set of lens parameters are automatically provided. The reconstructed B band HST image is shown in the lower-right panel of Figure 13. From this image we can see that the source in the rest frame UV consists of multiple components, including the main galaxy component and two clumps separated by 0.15 arcsec (i.e., 1.2 kpc in projected distance) indicated by the purple and red ellipses. The reconstructed H band HST image is shown in Figure 14. This image shows that the source in the rest-frame optical also consists of multiple components.

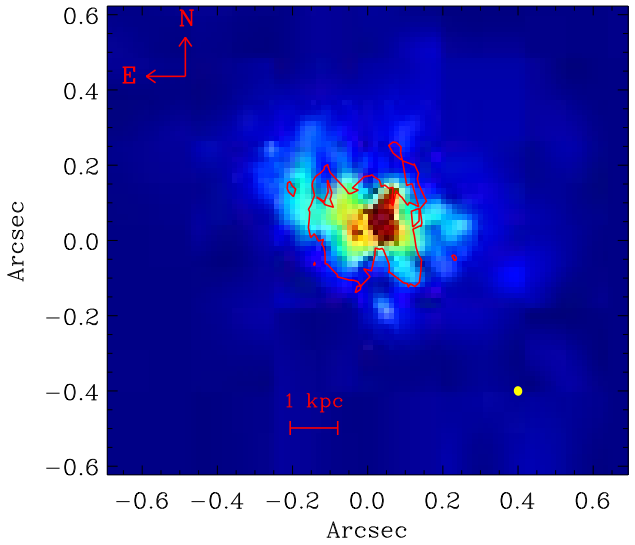

Figure 14. The reconstructed H band HST image is shown in the plot. From this image we can see that the source in the rest frame optical is formed of multiple components, two main galaxy components. The clump in the reconstructed UV image is partially resolved in this image and it shows a slightly different morphology. The contour shows the HST B-band reconstructed image. The yellow ellipse in the corner of the image shows the spatial resolution in the source plane.

5.1.1 *Reconstructed-*Hβ *and* [O II] *emission lines maps in the source plane*

Here we make use of the B band HST data modeling to reconstruct the Hβ and [O II] emission line maps of the galaxy. These lines have the highest signal-to-noise that we obtain from the SINFONI data.

For each spectral pixel image (frame) of the SINFONI data cubes, we derive the most probable source surface brightness distribution by keeping the lens parameters fixed at the best values recovered from the B band HST data modeling (after taking into account the rotation of the image), while re-optimizing for the source regularization level. Because of the relatively low signal-to-noise SINFONI data and non-homogenous sky background, we can not use all the lensed images. We focus instead on the highest magnification image, which is the A2 image.

Before reconstructing the Hβ map in the source plane, we first bin in the spectral direction by a factor of 4. This

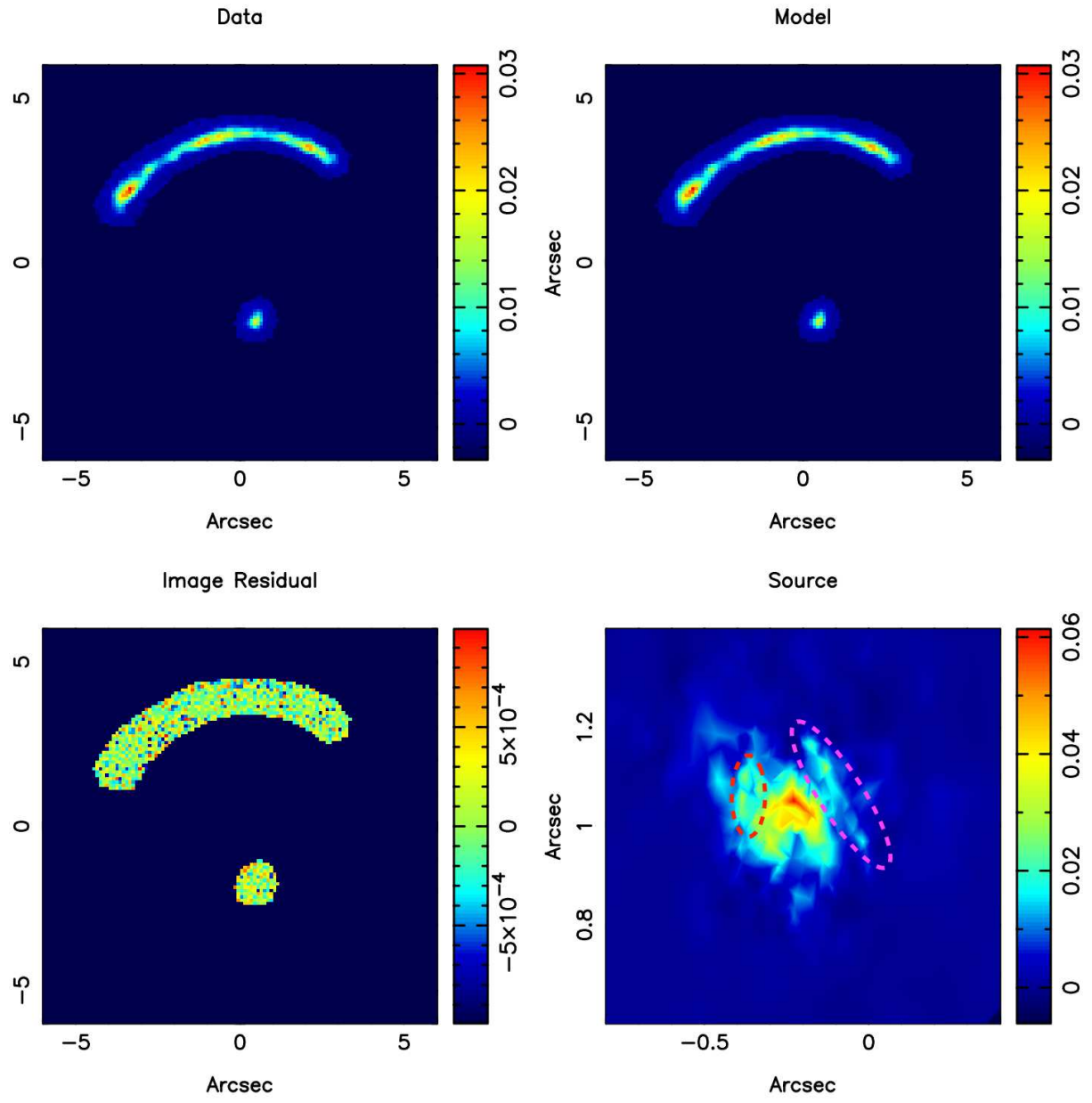

Figure 13. Top-left panel: the arc and the counter image in the B band HST image. The foreground galaxy (lens) has been removed from this image. Top-right panel: the best-fit model. Lower-left panel: the residuals after subtracting this model from the data. The reconstructed B band HST image is shown in the lower-right panel. From this image we see that the source in the rest frame UV consists of at least three components; the main galaxy component, a clump separated by $0.15''$, which is shown by the purple dashed ellipse and another clump separated by $0.15''$, which is shown by the red dashed ellipse.

corresponds to the spectral resolution (FWHM= 7.9 Å) that we measure from the line widths of the night sky lines around the Hβ line. This provides us with higher signal-to-noise image plane frames. We finally make a Hβ source cube from these reconstructed source frames and use that to derive the kinematics of the galaxy. A reconstructed Hβ map is shown in Figure 15. This image also shows two galaxy components. In order to better understand the morphology of the Hβ image, we divide the Hβ spectral range into three equal spectral bins defined as blue ($\lambda(4855-4859)$Å), green ($\lambda(4859-4863)$Å) and red ($\lambda(4863-4867)$Å) intervals, corresponding to three SFR maps shown in Figure 11. We then reconstruct the source surface brightness distribution for each of these images, using the same method that was used for the whole Hβ image. The three panels in Figure 16 show the reconstructed sources for these images. We can see that the west part of the Hβ line map is very weak and only dominates in the red image (right panel); on the other hand, the eastern part is dominant in the blue image (left panel). Figure 17 shows a reconstructed [O II] image of the galaxy. We see that the eastern component is dominant in this image. Here we are unable to separate the two components;

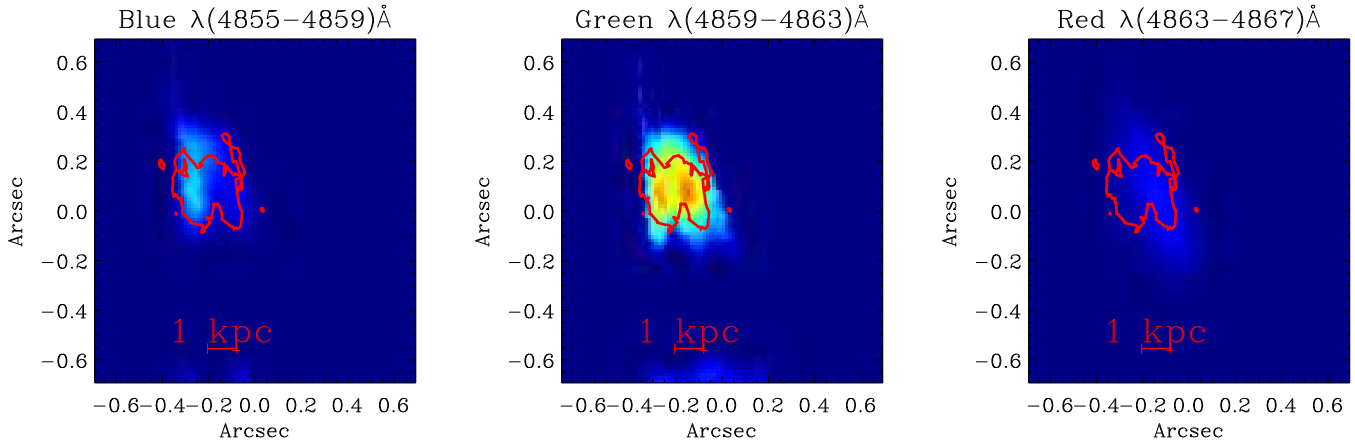

Figure 16. From left to right this figure shows reconstructed Hβ maps from the blue, green and red components of the spectral line. The contour line shows the reconstructed *HST B*-band image from Figure 13. It can be seen that the blue map predominantly contributes to the eastern part — from a detailed inspection of the lens model we find that in the image plane this is predominantly seen in the A1 and A2 images. Note also that the red component of the spectral line predominantly originates in the west.

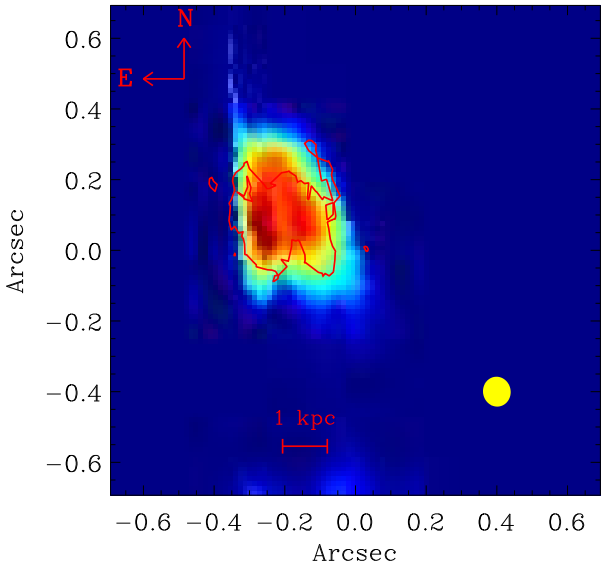

Figure 15. The reconstructed Hβ image is shown in the plot. From this image we can see that the source in the rest frame optical is formed of multiple components, two main galaxy components. The clump in the reconstructed UV image is not resolved in this image. The contour shows the reconstructed *HST B*-band image from Figure 13. The yellow ellipse in the corner of the image shows the spatial resolution in the source plane.

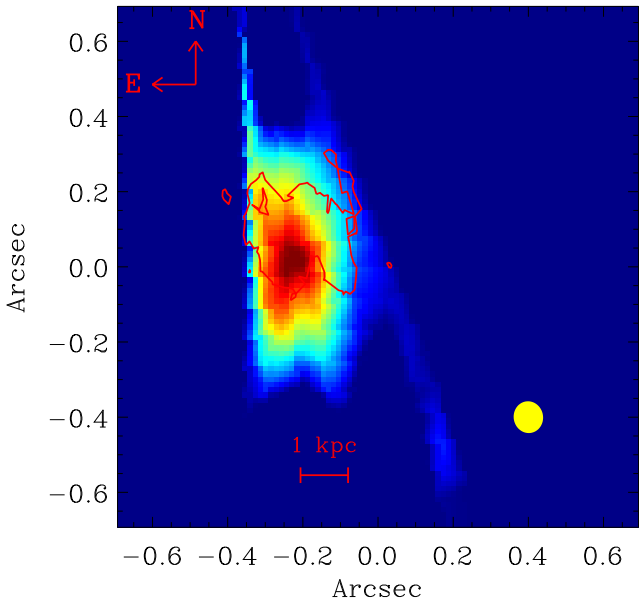

Figure 17. The reconstructed [O II] image. Here we are unable to separate two components; this might be due to a higher [O II] /Hβ ratio in the left component. The red contour shows the reconstructed *HST B*-band image from Figure 13.

this might be due to a higher [O II] /Hβ ratios in the eastern component, but could also be caused by the lower spatial resolution at these wavelengths. However, we rule out the later explanation by convolving the Hβ map with a Gaussian PSF matching the slightly different [O II] map (*J*-band) PSF.

5.2 Hβ profile of the reconstructed source

We use the same fitting method that we used in Section 3 to fit a two component Gaussian to the Hβ profile for every pixel. We also integrate over the total flux of the galaxy and fit a two component Gaussian to it to compare it to our study in the observed plane (see Section 3.2). Figure 18 shows the Hβ profile derived from the reconstructed Hβ source. We see that this profile also retains two components. The width of the Gaussian for both components is 1.59 Å, which gives

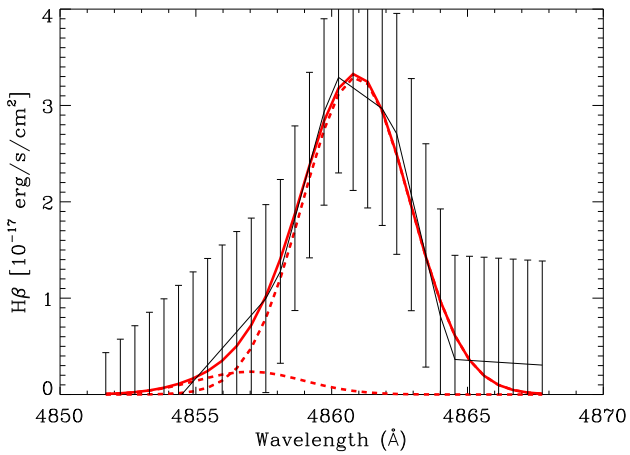

Figure 18. Hβ profile derived from the reconstructed Hβ source. The widths of both Gaussian components are 1.59 Å, which gives a velocity dispersion of 98 km s^{-1}. The velocity offset between the two components is 246 km s^{-1}. In the source plane, we have fewer bins than Figure 3, since we bin in spectral resolution by a factor 4 before reconstructing the Hβ map in the source plane. To make this profile, we interpolate between those bins to have the same binning as Figure 3.

a velocity dispersion of 98 ± 44 km s^{-1}. This is consistent, within the errors, with our estimated velocity dispersion for the A2 and A3 images in the observed plane (i.e., 104 ± 42 km s^{-1}). The velocity offset between the two components is 246 ± 46 km s^{-1} and matches the offset that we derive for the A2 and A3 images in the image plane. Figure 19 shows the velocity and velocity dispersion maps derived from the reconstructed Hβ source. From these maps, we see that the east galaxy component has a lower velocity and velocity dispersion relative to the western component. The western component also shows a smoother velocity gradient.

The Hβ line flux divided by the H-band continuum flux is shown as a proxy for EW(Hβ) in Figure 20. Here, the H-band continuum map is convolved to the same PSF as the Hβ map. From this we see that the outskirts of the galaxy show a clumpy and higher EW(Hβ). The eastern component of the galaxy also shows a higher EW(Hβ), which might be interpreted as a younger age relative to that of the main component.

6 DYNAMICS

6.1 Hβ Kinematics

To test whether the kinematics of the galaxy are consistent with those of a rotating disk, we compare the velocity and velocity dispersion maps derived from the reconstructed Hβ map with an exponential disk model. Given the low resolution and the low S/N of our data, we simulate a very simple system. The disk models is created using the *DYSMAL* IDL code (Davies et al. 2011, see also Cresci et al. 2009 for description of the code). The code was used extensively to derive intrinsic properties of disk galaxies (e.g., for estimating the dynamical mass of high-z galaxies; see Cresci et al. 2009). The code uses a set of input parameters which con-

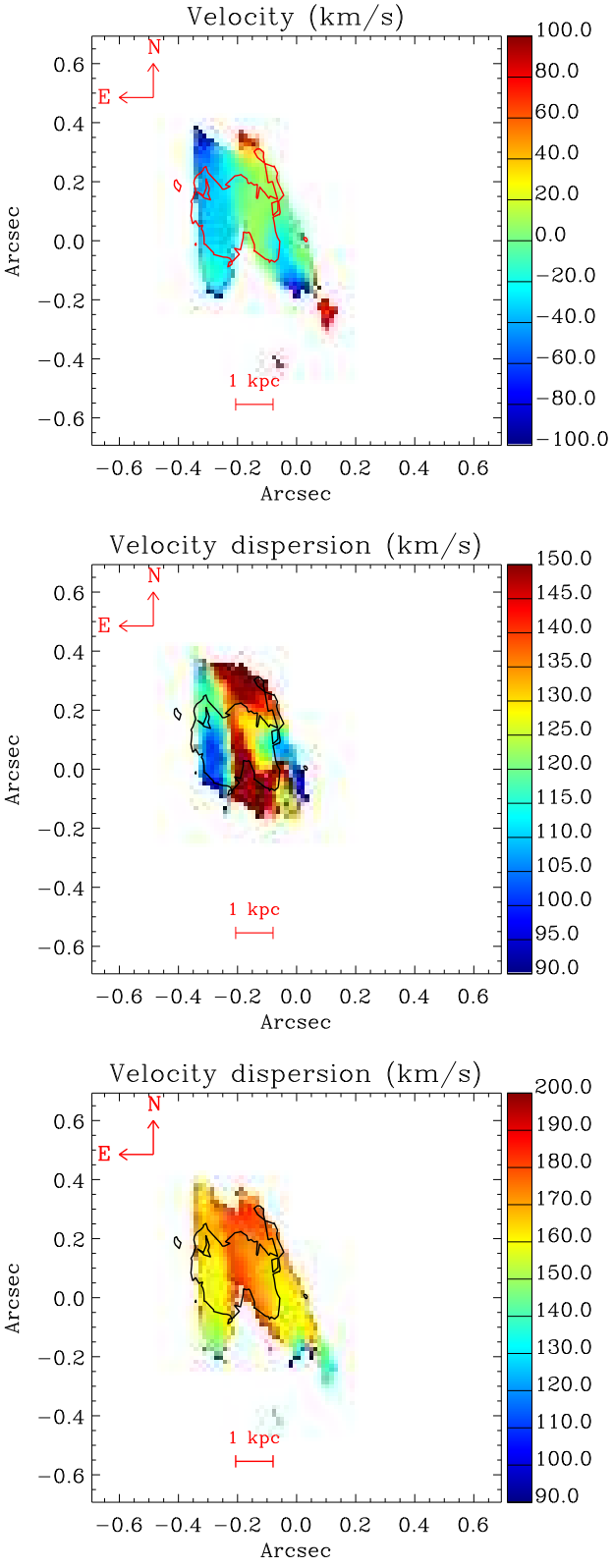

Figure 19. The top and middle panels show the velocity and velocity dispersion maps, respectively. The velocity map is derived using single Gaussian fits but velocity dispersion map represents both components. These are derived from the reconstructed Hβ source. The bottom panel shows the velocity dispersion map derived using single Gaussian fits. The contours show the reconstructed *HST* B-band image from Figure 13.

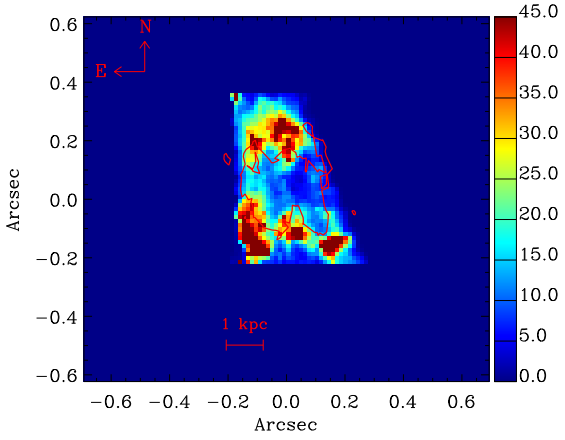

Figure 20. Hβ line flux divided by the H-band continuum flux shown as a proxy for EW(Hβ). We see that the outskirts of the galaxy show a clumpy and higher EW(Hβ). The eastern component of the galaxy shows a higher EW(Hβ), i.e., a younger age, relative to that of the main component. The red contour shows the reconstructed *HST* B-band image.

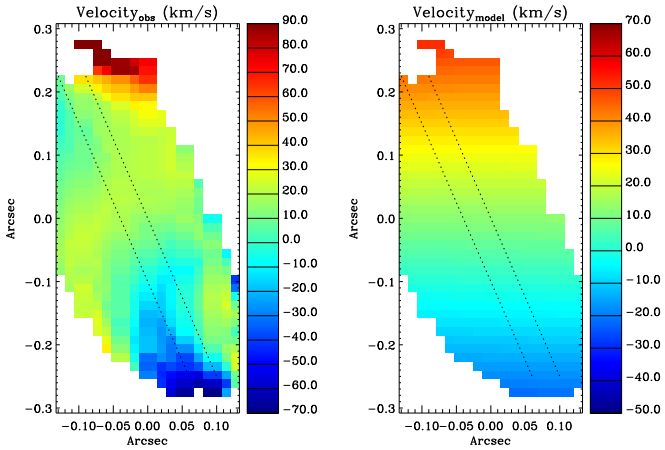

Figure 21. The left panel shows the observed velocity derived from the reconstructed Hβ map. The right panel shows the best velocity fit.

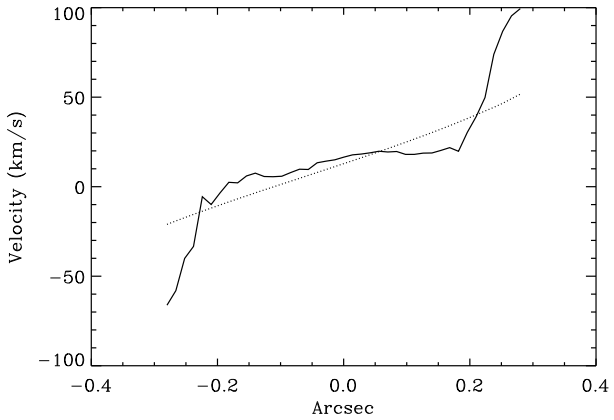

Figure 22. The observed velocity derived from the reconstructed Hβ map along the slit (shown by dashed lines in Figure 21) is shown by the solid curve. The dashed line here shows the best-fit velocity model.

strain the radial mass profile as well as the position angle and systemic velocity offset, in order to derive a 3D data cube with one spectral (i.e., velocity) and two spatial axes. This can be further used to extract kinematics. The best-fit disk parameters are derived using an optimized χ^2 minimization routine and the observed velocity and velocity dispersion. The mass extracted from *DYSMAL* is that of a thin disk model assuming supported only by orbits in ordered circular rotation.

We do not have any constraints on the inclination of our system. Therefore, we use a nominal inclination of 20 degrees. We account for spatial beam smearing from the PSF and velocity broadening due to the finite spectral resolution of the instrument and also rebin by a factor of 4 in the spectral direction in our modeling. We then compare this spatially and spectrally convolved disk model to the observations.

We focus on the western component in the velocity map shown in Figure 19 because from the lens modeling we know that this part contains the main component of the galaxy and also shows a smoother observed gradient. The best-fitting exponential disk model for this component is shown in Figure 21. While the disk model can reproduce some large-scale features of the velocity field, the residuals are substantial. We can therefore rule out a single rotating disk as a reasonable description of this system. We conclude that the 8 o'clock arc has a complex velocity field that cannot be explained by a simple rotating disk.

Furthermore, there appears to be a second component from a clump (see red ellipse in Figure 13) that partially overlaps with this component. Whether this is a sign of an on-going merger is difficult to ascertain with the present data. Indeed, the S/N in Hβ does not warrant a much more complex model to be fitted.

6.2 Dynamical mass

DZ11 estimated the dynamical mass of the 8 o'clock arc from the line widths via the relation presented by Erb et al. (2006b). We use the same method to estimate the dynamical mass using our estimated velocity dispersion (σ) and half-light radius. For rotation-dominated disks, DZ11 assumed that the enclosed dynamical mass within the half-light radius, $r_{1/2}$, is $M_{\rm dyn,rot}\,(r < r_{1/2}) = (2.25\sigma^2 r_{1/2})/G$ and multiply this resulting mass by two to obtain the total dynamical mass, where $G = 4.3 \times 10^{-6}\,{\rm kpc\,(km\,s^{-1})^2\ M_\odot^{-1}}$ is the gravitational constant. For dispersion-dominated objects, they applied the isotropic virial estimator with $M_{\rm dyn,disp} = (6.7\sigma^2 r_{1/2})/G$, appropriate for a variety of galactic mass distributions (Binney & Tremaine 2008). In this case, $M_{\rm dyn,disp}$ represents the total dynamical mass.

For estimating the half-light radius we run *galfit* on the reconstructed B and H band images. This gives us $r_{1/2} = 2.8 \pm 0.2$ kpc. We measure $\sigma = 104 \pm 42$ km s^{-1} and a rotation-dominated dynamical mass $\log\,(M_{dyn}/M_\odot) = 10.2 \pm 0.3$ and a dispersion-dominated dynamical mass

$\log(M_{dyn}/M_{\odot}) = 10.7 \pm 0.27$ (these values are corrected for instrumental broadening). Using the de-lensed spectra, we also estimate a $\sigma = 98 \pm 44$ km s^{-1}, which give us 10.1 ± 0.6, and 10.6 ± 0.6 for the rotation-dominated and dispersion-dominated dynamical masses, respectively. The disk model fit can also provide a dynamical mass estimate, $\log(M_{dyn}/M_{\odot}) = 9.5$, but we do not use this here because it only accounts for the west component of the velocity map.

We note that the idea of using a single line width to estimate dynamical mass is not convincing (this should be done for blue, green and red components individually). In that case the velocity field is clearly more like a merger, so neither of these dynamical mass indicators are reliable. Therefore, obtaining a robust dynamical mass estimate would require considerably more sophisticated models. The simple models are not physically constraining.

6.3 A massive outflow of gas?

It has been shown that many of high-z star-forming galaxies show evidence for powerful galactic outflows, indicated by studying UV absorption spectroscopy (Pettini et al. 2000; Shapley et al. 2003; Steidel et al. 2010; Weiner et al. 2009; Kornei et al. 2012) and broad Hα emission-line profiles (Shapiro et al. 2009; Genzel et al. 2011; Newman et al. 2012a). Recently Newman et al. (2012b) showed how galaxy parameters (e.g., mass, size, SFR) determine the strength of these outflows. They decomposed the emission line profiles into broad and narrow components and found that the broad emission is spatially extended over $\sim$ a few kpc. Newman et al. (2012b) showed that star formation surface density enforces a threshold for strong outflows occurring at 1 M$_{\odot}$ yr^{-1} kpc^{-2}. The threshold necessary for driving an outflow in local starbursts is 0.1 M$_{\odot}$ yr^{-1} kpc^{-2} (Heckman 2002).

The 8 o'clock arc with integrated star formation surface density of 9.2 M$_{\odot}$ yr^{-1} kpc^{-2} is certainly in the regime of strong outflow. If we consider the ratio of the Gaussian flux in the blue-shifted component to that of the main component (~ 0.5) as the F_{broad}/F_{narrow}, then our result is consistent with what Newman et al. (2012b) show in their Figure 2. However, we note that this definition is not exactly what Newman et al. (2012b) introduced as F_{broad}/F_{narrow} as we do not fit broad and narrow components but two component with the same width. This provides us with a lower limit on the line width of the blue shifted component.

In our data we find a blue-shifted component to Hβ as discussed in Section 3.2. As we mentioned earlier we used the same Gaussian width for both main and blue-shifted components. Given the low SN, a unique broad fit with a physical meaning can not be found considering the fact that residual from sky lines might create broad line widths. The velocity offset between this component and the main component of the Hβ line is ≈ 190 km s^{-1} for the A2 image and ≈ 280 km s^{-1} for the A3 image. This blue-shifted component could be due to an outflow of gas or a minor merger.

In support of the outflow picture, Finkelstein et al. (2009) and DZ10 both observed that ISM lines in the rest-UV spectrum of the 8 o'clock arc are blue-shifted relative to the stellar photospheric lines. They also argued that this was a sign of an outflow of gas from the galaxy and taken together with the SINFONI results this strengthens the outflow picture. A further argument for an outflow is the fact that as we saw in section 4.7, the H II regions have an elevated internal pressure, at least compared to similar galaxies locally, and it is reasonable to assume that this aids in driving an outflow (Heckman et al. 1990). In support of the merger picture, Figure 16 indicates that much of the blue component flux is extended and arguably galaxy shaped.

Taking the evidence from the UV ISM lines, the Hβ profile, the lens model and the high ISM pressure together, it is likely that there is a significant outflow component to the blue-shifted wing, but the question here is whether these observations correspond to a reasonable amount of gas in the outflow. To answer this we also estimate the mass of ionized hydrogen from the luminosity of Hβ, $L_{\mathrm{H}\beta}$, of the blue-shifted component and main component of the 8 o'clock arc using (e.g., Dopita & Sutherland 2003):

$$M_{\mathrm{ionised}} = \frac{m_{\mathrm{H}} \times L_{\mathrm{H}\beta}}{1.235 \times 10^{-25} T_4^{-0.86} n_e}, \quad (3)$$

where m_{H} is the mass of the hydrogen atom, T_4 the electron temperature in units of 10,000 K and n_e the electron density. The mass of ionized hydrogen for the blue-shifted component with $L_{\mathrm{H}\beta}$ of 45×10^{41}erg s^{-1} is $10^{7.7\pm1.3}$ $M_{\odot}$ assuming $n_e = 600$ cm^{-3}, which can be contrasted with the mass of ionized hydrogen in the main component which is $10^{8.2\pm1.3} M_{\odot}$ (with $L_{\mathrm{H}\beta} = 127 \times 10^{41}$erg s^{-1}). The estimate for the blue-shifted component is clearly an upper limit because from the argument above it seems likely that the blue component is not purely an outflow. Thus, taking this at face value, we would find that with an outflow rate of 10% of the star formation rate, a conservative value given local observations (e.g., Martin 1999, 2006), we need the current star formation activity to have lasted $< 3 \times 10^8$ yr, which is not unreasonable (to estimate the star formation time scale, the mass is divided by 10% of the SFR).

In order to use the outflow mass quantitatively, we need to have an estimate of outflow mass in neutral hydrogen. However, we note that we can not estimate this for the blue-shifted component since N_{HI} estimated in DZ10 is given for the whole galaxy. To estimate the total neutral hydrogen mass in the outflow and the mass outflow rate (Pettini et al. 2000), we use the following formulae given in Verhamme et al. (2008)

$$M_{\mathrm{HI}} \approx 10^7 \left(\frac{r}{1\ \mathrm{kpc}}\right)^2 \left(\frac{N_{\mathrm{HI}}}{10^{20}\mathrm{cm}^{-2}}\right) M_{\odot}, \quad (4)$$

$$\dot{M}_{\mathrm{HI}} = 6. \left(\frac{r}{1\ \mathrm{kpc}}\right)\left(\frac{N_{\mathrm{HI}}}{10^{20}\mathrm{cm}^{-2}}\right)\left(\frac{V_{exp}}{200\ \mathrm{km\ s}^{-1}}\right) M_{\odot}\ yr^{-1}, \quad (5)$$

where the first equation relate H I mass in the shell to its column density N_{HI} and the second equation assumes that the mechanical energy deposited by the starburst has produced a shell of swept-up interstellar matter that is expanding with a velocity of V_{exp}.

Assuming our estimated half-light radius from the rest-frame UV reconstructed image and our assumed outflow velocity ($r = 2.8$ kpc, $V_{exp} = 200$ km s^{-1}) and taking $N_{\mathrm{HI}} = 10^{20.57}$ cm^{-2} from DZ10, we find neutral gas masses of $M_{\mathrm{HI}} = 2.9 \times 10^8 M_{\odot}$ and an outflow rate of $\dot{M}_{\mathrm{HI}} = 62.4\ M_{\odot}\ yr^{-1}$. This gives us a mass-loading factor of $\eta = \dot{M}_{\mathrm{HI}}/\mathrm{SFR} = 0.27$.

7 CONCLUSIONS

We present a spatially-resolved analysis of the 8 o'clock arc using near-IR IFU data. From this we recovere the Hβ map and the spatially-resolved Hβ profile. We showed that Hβ has different profiles at different spatial pixels and is composed of multiple components. We carefully modeled the strong emission lines in the galaxy and compared the results to a local comparison sample. This allowed us to conclude that

- The 8 o'clock arc lies on the same M_*-O/H-SFR manifold as similar star-forming galaxies locally (Mannucci et al. (2010); Lara-López et al. (2010), DZ11).
- The gas surface density in the 8 o'clock arc $\log(\Sigma_{\rm gas}/\ {\rm M}_\odot\ {\rm pc}^{-2}) = 1.6^{1.87}_{1.46}$ is more than twice ($\times 2.16^{4.01}_{1.55}$) that of similar galaxies locally $\log(\Sigma_{\rm gas_{(analogs)}}/\ {\rm M}_\odot\ {\rm pc}^{-2}) = 1.27^{1.48}_{1.02}$. Comparing this with other high-z results (e.g., Mannucci et al. 2009, who measure gas surface densities in the range of 2.5-3.3 ${\rm M}_\odot\ {\rm pc}^{-2}$), the gas surface density for the 8 o'clock arc is lower. Note that as mentioned by Mannucci et al. (2009), they are sampling the central, most active parts of the galaxies, so those values should be considered as the maximum gas surface densities.
- The electron density, and thus the H II region pressure, in the 8 o'clock arc is ~ 5 times that of similar galaxies locally. As (Wuyts et al. 2012) pointed out, the electron density measurements for high-z galaxies range from the low density limit to $n_e > 10^4\ {\rm cm}^{-3}$. Although these differences depend on the method for measuring the electron density, these also imply a huge difference in the physical properties of star-forming regions in star-forming galaxies at $z \sim 2$. The difference between electron density at low-z and high-z have been studied recently by Shirazi et al. (2013, submitted) who compared a sample of 14 high-z galaxies with their low-z counterparts in the SDSS and showed that high-z star-forming galaxies that have the same mass and sSFR as low-z galaxies have a median of 8 times higher electron densities.

Taken together these results imply that although the 8 o'clock arc seems superficially similar to local galaxies with similar mass and star formation activity, the properties of the ISM in the galaxy are nonetheless noticeably different.

We showed that the two images A2 and A3 have the same Hβ profiles, which of course is to be expected because they are two images of the same galaxy. But this contrasts with the results from long-slit observations of the object by DZ11 who found different profiles. The similarity of the profiles from the IFU data has allowed us to rule out a significant contribution of substructures to the surface brightness of the A2 image.

The integrated Hβ profile of both images show a main component with a blue wing which can be fitted by another Gaussian profile with the same width. The width of the Gaussian components for both images are 1.7 ± 0.7 Å, which gives velocity dispersion $\sim 104 \pm 42$ km s^{-1}. The velocity offset between the two components is 278 ± 63.5 km s^{-1} for the A3 image and 191 ± 63 km s^{-1} for the A2 image which are consistent within the errors. Since both DZ11 and Finkelstein et al. (2009) showed ISM lines are blue-shifted relative to the stellar photospheric lines, suggesting gas outflows with 120-160 km s^{-1}, and find a comparatively high pressure in the H II regions of the 8 o'clock arc, we interpret this blue-shifted component as an outflow. However, we cannot rule out that the blue-shifted component might represent a minor merger.

To study the de-lensed morphology of the galaxy, we used existing B and H band HST images. Based on this, we constructed a rigorous lens model for the system using the Bayesian grid based lens modeling technique. In order to obtain a robust lens model, we used the lens modeling of the B band HST image to reconstruct the Hβ line map of the galaxy. We then presented the de-lensed Hβ line map, velocity and velocity dispersion maps of the galaxy. As an example application we derived the Hβ profile of the reconstructed source and showed that this also requires two Gaussian components with a width of 98 ± 44 km s^{-1} and velocity separation of 246 ± 46 km s^{-1}.

By fitting an exponential disk model to the observed velocity field, we showed that a simple rotating disk cannot fit the velocity field on its own. Thus, a more complex velocity field is needed, but the S/N of the present data does not allow a good constraint to be had. This also implies that obtaining an accurate dynamical mass for the 8 o'clock system is not possible at present.

Similar to some of clumpy galaxies studied by Genzel et al. (2011), the 8 o'clock arc shows a blue-shifted wing but with a less broad profile. We note that as can be seen for example from Figure 13, the galaxy has a very clumpy nature in the source plane, but because of the lack of spatial resolution we are not able to study these clumps in more detail.

ACKNOWLEDGEMENTS

We are very thankful for useful comments and suggestions of the anonymous referee. We would like to thank also Ali Rahmati for his useful comments on this paper, Raymond Oonk and Benoit Epinat for useful discussion about SINFONI data reduction, Richard Davies for providing us with DYSMAL code, Johan Richard for his help on the lens modeling and also Max Pettini, Alicia Berciano Alba,Thomas Martinsson and Joanna Holt for useful discussions.

We would like also to express our appreciation to Huan Lin, Michael Strauss, Chris Kochanek, Alice Shapley, Dieter Lutz, Chuck Steidel, and Christy Tremonti for their help on the HST proposal along with our spacial thanks to Andrew Baker.

M. Sh., S. A. and D. T. acknowledge the support of Mel Ulmer at North Western University for providing them a meeting room and working place in May-June 2011.

S.V. is grateful to John McKean for useful comments and discussions on the lens modeling

During part of this work S.V. was supported by a Pappalardo Fellowship at MIT.

This research has made use of the Interactive Data Language (IDL) and QFitsView[5].

[5] www.mpe.mpg.de/∼ott/QFitsView

REFERENCES

Allam, S. S., Tucker, D. L., Lin, H., Diehl, H. T., Annis, J., Buckley-Geer, E. J., & Friemam, J. A. 2007, ApJ, 662, L51

Baldwin, J. A., Phillips, M. M., & Terlevich, R. 1981, PASP, 93, 5

Binney, J., & Tremaine, S. 2008, Galactic Dynamics, 2nd Edition, Princeton University Press, Princeton, NJ USA

Bonnet, H., Conzelmann, R., Delabre, B., et al. 2004, Proc. SPIE, 5490, 130

Bouché, N., Cresci, G., Davies, R., et al. 2007, ApJ, 671, 303

Brinchmann, J., Charlot, S., et al. 2004, MNRAS, 351, 1151

Brinchmann, J., Charlot, S., Kauffmann, G., et al. 2013, MNRAS, 1276

Bruzual, G., & Charlot, S. 2003, MNRAS, 344, 1000

Chabrier, G. 2003, PASP, 115, 763

Charlot, S., Longhetti, M., 2001, MNRAS, 323, 887

Contini, T., Garilli, B., Le Fèvre, O., et al. 2012, A & A, 539, A91

Cresci, G., Hicks, E. K. S., Genzel, R., et al. 2009, APJ, 697, 115

Davies, R., Förster Schreiber, N. M., Cresci, G., et al. 2011, APJ, 741, 69

de Barros, S., Schaerer, D., & Stark, D., 2012, arXiv:1207.3663

Dessauges-Zavadsky, M., D'Odorico, S., Schaerer, D., Modigliani, A., Tapken, C., & Vernet, J. 2010, A&A, 510, 26

Dessauges-Zavadsky, M., Christensen, L., D'Odorico, S., Schaerer, D., & Richard, J. 2011, A & A, 533, A15

Dopita, M. A. & Sutherland, R. S. 2003, Astrophysics of the diffuse universe (Astrophysics of the diffuse universe, Berlin, New York: Springer, 2003. Astronomy and astrophysics library, ISBN 3540433627)

Dopita, M. A., Fischera, J., Sutherland, R. S., et al. 2006, APJS, 167, 177

Dopita, M. A., Fischera, J., Sutherland, R. S., et al. 2006, APJ, 647, 244

Eisenhauer, F., Abuter, R., Bickert, K., et al. 2003, Proc. SPIE, 4841, 1548

Eldridge, J. J., & Stanway, E. R. 2012, MNRAS, 419, 479

Erb, D. K., Shapley, A. E., Pettini, M., Steidel, C. C., Reddy, N. A., & Adelberger, K. L. 2006a, ApJ, 644, 813

Erb, D. K., Steidel, C. C., Shapley, A. E., Pettini, M., Reddy, N. A., & Adelberger, K. L. 2006b, ApJ, 646, 107

Erb, D. K., Steidel, C. C., Shapley, A. E., Pettini, M., Reddy, N. A., & Adelberger, K. L. 2006c, ApJ, 647, 128

Epinat, B., Tasca, L., Amram, P., et al. 2012, A & A, 539, A92

Finkelstein, S. L., Papovich, C., Rudnick, G., Egami, E., Le Floc'h, E., Rieke, M. J., Rigby, J. R, & Willmer, C. N. A. 2009, ApJ, 700, 376

Fïster Schreiber, N. M., Genzel, R., Lehnert, M. D., et al. 2006, ApJ, 645, 1062

Förster Schreiber, N. M., Genzel, R., Bouché, N., et al. 2009, ApJ, 706, 1364

Förster Schreiber, N. M., Shapley, A. E., Erb, D. K., et al. 2011, APJ, 731, 65

Förster Schreiber, N. M., Shapley, A. E., Genzel, R., et al. 2011, APJ, 739, 45

Gallazzi, A., Charlot, S., et al., 2005, MNRAS, 362, 41

Gallazzi, A., Brinchmann, J., et al., 2008, MNRAS, 383, 1439

Genzel, R., Tacconi, L. J., Eisenhauer, F., et al. 2006, Nature, 442, 786

Genzel, R., Burkert, A., Bouché, N., et al. 2008, ApJ, 687, 59

Genzel, R., Tacconi, L. J., Gracia-Carpio, J., et al. 2010, MNRAS, 407, 2091

Genzel, R., Newman, S., Jones, T., et al., 2011, ApJ, 733, 101

Gnerucci, A., Marconi, A., Cresci, G., et al. 2011, A & A, 528, A88

Heckman, T. M. 2002, Extragalactic Gas at Low Redshift, ed. J. S. Mulchaey & J. Stocke (San Francisco, AC: ASP), 254, 292

Jones, T. A., Swinbank, A. M., Ellis, R. S., Richard, J., & Stark, D. P. 2010, MNRAS, 404, 1247

Jones, T., Ellis, R., Jullo, E., & Richard, J. 2010, APJL, 725, L176

Heckman, T. M., Armus, L., & Miley, G. K. 1990, APJS, 74, 833

Kauffmann, G., Heckman, T.M., et al. 2003, MNRAS, 346, 1055

Kennicutt, R. C., Jr. 1992, APJ, 388, 310

Kennicutt, R. C., Jr. 1998, ARA&A, 36, 189

Kewley, L. J. & Ellison, S. L. 2008, ApJ, 681, 1183

Kornei, K. A., Shapley, A. E., Martin, C. L., et al. 2012, APJ, 758, 135

Krist, J. E., Hook, R. N., & Stoehr, F. 2011, Proc. SPIE, 8127

Lara-López, M. A., Cepa, J., Bongiovanni, A., et al. 2010, A & A, 521, L53

Lamareille, F., Contini, T., Le Borgne, J.-F., et al. 2006, A & A, 448, 893

Law, D. R., Steidel, C. C., Erb, D. K., Larkin, J. E., Pettini, M., Shapley, A. E., & Wright, S. A. 2007, ApJ, 669, 929

Lehnert, M. D., Nesvadba, N. P. H., Le Tiran, L., et al. 2009, APJ, 699, 1660

Lehnert, M. D., Le Tiran, L., Nesvadba, N. P. H., et al. 2013, arXiv:1304.7734

Le Tiran, L., Lehnert, M. D., van Driel, W., Nesvadba, N. P. H., & Di Matteo, P. 2011, A & A, 534, L4

Maiolino, R., Nagao, T., Grazian, A., et al. 2008, A&A, 488, 463

Mannucci, F., Cresci, G., Maiolino, R., et al. 2009, MNRAS, 398, 1915

Mannucci, F., Cresci, G., Maiolino, R., Marconi, A., & Gnerucci, A. 2010, MNRAS, 408, 2115

Martin, C. L. 1999, APJ, 513, 156

Martin, C. L. 2005, APJ, 621, 227

Martin, C. L. 2006, APJ, 647, 222

Martin, C. L., Shapley, A. E., Coil, A. L., et al. 2012, APJ, 760, 127

Moustakas, J., Kennicutt, R. C., Jr., & Tremonti, C. A. 2006, APJ, 642, 775

Nesvadba, N. P. H., Lehnert, M. D., Eisenhauer, F., et al. 2006, APJ, 650, 661

Nesvadba, N. P. H., Lehnert, M. D., Eisenhauer, F., et al. 2006, APJ, 650, 693

Nesvadba, N. P. H., Lehnert, M. D., Genzel, R., et al. 2007, APJ, 657, 725

Nesvadba, N. P. H., Lehnert, M. D., De Breuck, C., Gilbert, A., & van Breugel, W. 2007, A & A, 475, 145
Newman, S. F., Shapiro Griffin, K., Genzel, R., et al. 2012, APJ, 752, 111
Newman, S. F., Genzel, R., Förster-Schreiber, N. M., et al. 2012, APJ, 761, 43
Newman, S. F., Genzel, R., Förster Schreiber, N. M., et al. 2013, APJ, 767, 104
Osterbrock, D. E. 1989, Astrophysics of gaseous nebulae and active galactic nuclei, University Science Books, Mill Valley, CA USA
Pettini, M., & Pagel, B. E. J. 2004, MNRAS, 348, 59
Pettini, M., Rix, S. A., Steidel, C. C., Adelberger, K. L., Hunt, M. P., & Shapley, A. E. 2002, ApJ, 569, 742
Pettini, M., Steidel, C. C., Adelberger, K. L., Dickinson, M., & Giavalisco, M. 2000, ApJ, 528, 96
Richard, J., Jones, T., Ellis, R., Stark, D. P., Livermore, R., & Swinbank, M. 2011, MNRAS, 413, 643
Schaerer, D., & de Barros, S. 2009, A&A, 502, 423
Schaerer, D., & de Barros, S. 2010, A&A, 515, 73
Salpeter, E. E. 1955, ApJ, 121, 161
Savaglio, S., Glazebrook, K., Le Borgne, D., et al. 2005, ApJ, 635, 260
Savaglio, S., Panagia, N., & Padovani, P. 2002, ApJ, 567, 702
Shapiro, K. L., Genzel, R., Quataert, E., et al. 2009, APJ, 701, 955
Shapley, A. E., Steidel, C. C., Pettini, M., & Adelberger, K. L. 2003, ApJ, 588, 65
Shapley, A. E., Steidel, C. C., Pettini, M., Adelberger, K. L., & Erb, D. K. 2006, APJ, 651, 688
Shapley A., 2011, ARA&A, 49, 525
Shapley, A. E., Steidel, C. C., Erb, D. K., et al. 2005, APJ, 626, 698
Schlegel, D. J., Finkbeiner, D. P., & Davis, M. 1998, ApJ, 500, 525
Shirazi, M., & Brinchmann, J. 2012, MNRAS, 421, 1043
Shirazi, M., & Brinchmann, J., Rahmati, A., 2013, Submitted
Schmidt M., 1959, APJ, 129, 243
Siana, B., Teplitz, H. I., Chary, R.-R., Colbert, J., & Frayer, D. T. 2008, APJ, 689, 59
Stark, D. P., Auger, M., Belokurov, V., et al. 2013, arXiv:1302.2663
Steidel, C. C., Adelberger, K. L., Shapley, A. E., et al. 2003, APJ, 592, 728
Steidel, C. C., Erb, D. K., Shapley, A. E., et al. 2010, APJ, 717, 289
Swinbank, A. M., Webb, T. M., Richard, J., et al. 2009, MNRAS, 400, 1121
Teplitz, H. I., McLean, I. S., Becklin, E. E., et al. 2000, ApJ, 533, L65
Tody, D. 1993, Astronomical Data Analysis Software and Systems II, 52, 173
Tremonti, C. A., Heckman, T. M., Kauffmann, G., et al. 2004, APJ, 613, 898
Vegetti, S., & Koopmans, L. V. E. 2009, MNRAS, 392, 945
Verhamme, A., Schaerer, D., Atek, H., & Tapken, C. 2008, A & A, 491, 89
Volino, F., Wucknitz, O., McKean, J. P., & Garrett, M. A. 2010, A & A, 524, A79
Weiner, B. J., Coil, A. L., Prochaska, J. X., et al. 2009, APJ, 692, 187
Wuyts, E., Rigby, J. R., Sharon, K., & Gladders, M. D. 2012, APJ, 755, 73
Yee, H. K. C., Ellingson, E., Bechtold, J., Carlberg, R. G., & Cuillandre, J.-C. 1996, AJ, 111, 1783

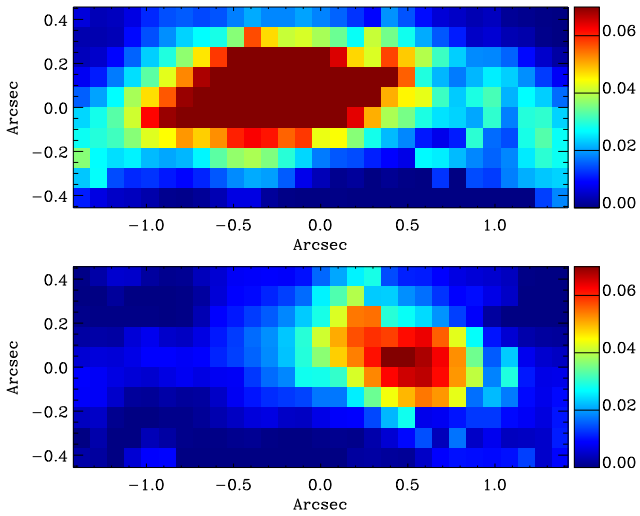

Figure A1. Lensed image A2: upper panel shows the Gaussian intensity map of the main component; lower panel shows the Gaussian intensity map of the blue-shifted component. Intensities are in unit of 10^{-17}erg cm^{-2} s^{-1}.

APPENDIX A: GAUSSIAN DECOMPOSITION

As we have shown in Section 3.3, the resolved Hβ profiles are not well fitted by a single Gaussian. Here we show the best-fit Gaussian intensity maps of the main and blue-shifted components of the galaxy for the image A2 and A3 in Figure A1 and Figure A2, respectively. As we mentioned earlier, during the fitting we require the lines to have the same velocity widths. In both figures, the upper panel shows the Gaussian intensity map of the main component and the lower panel shows the Gaussian intensity map of the blue-shifted component. Intensities are in unit of 10^{-17}erg cm^{-2} s^{-1}. We see that the main and the blue-shifted components of the galaxy are offset spatially ($\sim 1''$) in the A2 image as we see also in Figure 11 showing three calculated SFR maps of the A2 image in blue, green and red channels. However, for the A3 image it is not possible to decompose these components spatially.

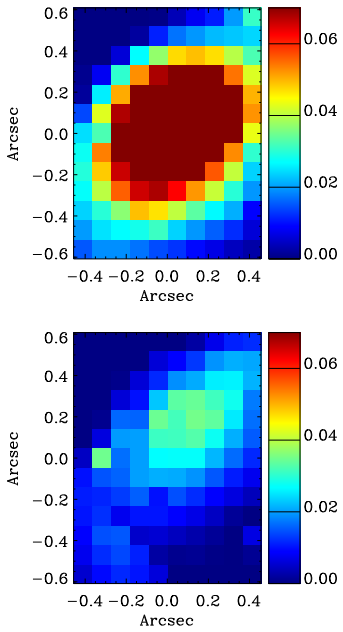

Figure A2. Lensed image A3: upper panel shows the Gaussian intensity map of the main component; lower panel shows the Gaussian intensity map of the blue-shifted component. Intensities are in unit of 10^{-17}erg cm^{-2} s^{-1}.